Post-outburst chemistry in a Very Low-Luminosity Object: Peculiar high abundance of nitric oxide

(article starts on next page)

Astronomy & Astrophysics

Post-outburst chemistry in a Very Low-Luminosity Object

Peculiar high abundance of nitric oxide

B. M. Kulterer[1,2,★], S. F. Wampfler[2], N. F. W. Ligterink[3,4], N. Murillo[5,6], T. -H. Hsieh[7], M. K. McClure[8], A. Boogert[9], K. Kipfer[3], P. Bjerkeli[10], and M. N. Drozdovskaya[2,11]

[1] Center for Astrophysics | Harvard & Smithsonian, Cambridge, MA 02138 USA
[2] Center for Space and Habitability, Universität Bern, Gesellschaftsstrasse 6, 3012 Bern, Switzerland
[3] Space Research & Planetary Sciences, Physics Institute, University of Bern, 3012 Bern, Switzerland
[4] Faculty of Aerospace Engineering, Delft University of Technology, Delft, The Netherlands
[5] Instituto de Astronomía, Universidad Nacional Autónoma de México, AP106, Ensenada, CP 22830, B.C., Mexico
[6] Star and Planet Formation Laboratory, RIKEN Cluster for Pioneering Research, Wako, Saitama 351-0198, Japan
[7] Max Planck Institut für Extraterrestrische Physik (MPE), Giessenbachstrasse 1, 85748 Garching, Germany
[8] Leiden Observatory, Leiden University, PO Box 9513, NL–2300, RA Leiden, The Netherlands
[9] Institute for Astronomy, University of Hawai'i at Manoa, 2680 Woodlawn Drive, Honolulu, HI 96822, USA
[10] Chalmers University of Technology, Department of Space, Earth and Environment, 412 96 Gothenburg, Sweden
[11] Physikalisch-Meteorologisches Observatorium Davos und Weltstrahlungszentrum (PMOD/WRC), Dorfstrasse 33, CH-7260 Davos Dorf, Switzerland

ABSTRACT

Context. Very Low Luminosity Objects (VeLLOs) are deeply embedded, and extremely faint objects ($L_{int} < 0.1\,L_\odot$), and are thought to be in the quiescent phase of the episodic accretion process. They fill an important gap in our understanding of star formation.
Aims. The VeLLO in the isolated DC3272+18 cloud has undergone an outburst in the past $\sim 10^4$ yr, and is thus an ideal target for investigating the chemical inventory in the gas phase of an object of its type. The aim of this study is to investigate the direct impact of the outburst on the chemical processes in the object and identify molecules that can act as tracers of past heating events.
Methods. Observations with the Atacama Pathfinder EXperiment (APEX) in four spectral windows in the frequency range of 213.6–272.4 GHz have been carried out to identify molecules that can be directly linked to the past outburst; to utilize the line fluxes, column densities, and the abundance ratios of the detected species to characterize the different physical components of the VeLLO; and to probe for the presence of complex organic molecules.
Results. Nitric oxide (NO) is detected for the first time in a source of this type, and its formation could be induced by the sublimation of grain-surface species during the outburst. In addition, the observations securely detect CH_3OH, H_2CO, D_2CO, SO, SO_2, CO, ^{13}CO, $C^{18}O$, N_2D^+, HCO^+, DCO^+, HCN, DCN, HNC, c-C_3H_2, and C_2D. The upper state energies of the securely detected lines and their derived line intensity ratios indicate that most of the probed material stems from regions of cold gas in the envelope enshrouding the VeLLO in the DC3272+18 cloud with a temperature of ~ 10 K. In addition, c-C_3H_2 traces a second, warmer gas reservoir with a temperature of ~ 35 K. The high D/H ratio derived from D_2CO points toward its origin from the prestellar stage, while deuteration of the gas-phase species DCO^+, DCN, and C_2D could still be ongoing in the gas in the envelope.
Conclusions. The gas probed by the observations already cooled down after the past heating event caused by the outburst, but it still has lasting effects on the chemistry in the envelope of the VeLLO. CH_3OH, H_2CO, SO, SO_2, and CO sublimated from grains during the outburst and have not fully frozen out yet, which indicates that the outburst took place $<10^4$ yr ago. A pathway to form NO directly in the gas phase is from the photodissociation products created after the sublimation of H_2O and NH_3 from the ices. While the present time water snowline has likely retreated to a pre-outburst small radius, the volatile NO species is still extensively present in the gas phase, as is evident by its high column density relative to methanol in the observations. This suggests that NO could be potentially used to trace the water snowline in outbursting sources. In order to rule out nonthermal desorption processes that could also have led to the formation of NO, this proposition has to be verified with future observations at a higher spatial resolution, and by searching for NO in additional targets.

Key words. astrochemistry – stars: formation – stars: low-mass – ISM: abundances – ISM: individual objects: DC3272+18

1. Introduction

Very Low Luminosity Objects (VeLLOs) were first identified by the "Cores to Disk" (c2D) legacy survey of the *Spitzer* Space Telescope (Evans et al. 2003; Young et al. 2004), and have been classified as protostellar objects that are deeply embedded

in molecular clouds with an internal luminosity of $\leq 0.1\,L_\odot$ (Young et al. 2004; di Francesco & Evans 2007). The nature and the future evolution of VeLLOs are currently under debate, as only a small number of sources have been studied in detail, because their low luminosity makes observations challenging. Their low internal luminosity suggests that they could be either young Class 0 sources (e.g., IRAM 04191: André et al. 1999; Dunham et al. 2006; L1521F: Bourke et al. 2006;

★ Corresponding author; beatrice.kulterer@cfa.harvard.edu

Cha-MMS1: Belloche et al. 2006; Väisälä et al. 2014; IRAS 16253: Hsieh et al. 2015, 2018), or even extremely low-mass protostars or proto-brown dwarf candidates (e.g., L328: Lee et al. 2009, 2013 ; L1148: Kauffmann et al. 2011; IC 348-SMM2E: Palau et al. 2014). One hypothesis is that VeLLOs are objects in the quiescent phase of the episodic accretion process. Studies as carried out for L673-7 (Dunham et al. 2010a), and for L1521F (Takahashi et al. 2013) have derived average mass accretion rates from the outflows of these objects that are a few times higher than their current internal luminosity allows for. Moreover, the aforementioned objects that were studied have bolometric temperatures and spectral energy distributions that are similar to protostars. However, their luminosities are significantly fainter than the luminosity that would be expected for the least massive protostars in standard star formation models with a constant mass accretion rate (Shu et al. 1987; Dunham et al. 2006). Episodic accretion could bypass this issue, if outbursts boost the accretion rate for short periods of time, before the objects return back to a more quiescent phase that is accompanied by less efficient mass accretion. The internal average luminosity of such objects would thus be lower than for an object with a constant mass accretion rate (Kenyon & Hartmann 1995; Dunham et al. 2010b).

While detailed studies of the physical properties of VeL-LOs are rare, even less is known about the chemistry in sources of this type. VeLLOs are faint objects, they are usually studied with typical molecular tracers such as CO and its isotopologues, N_2H^+ or HCN to quantify their large-scale structures and system properties (e.g., Hsieh et al. 2018; Kim et al. 2019, 2021). Species with a higher degree of complexity are rarely observed. Complex organic molecules (COMs; carbon-bearing species consisting of at least six atoms; Herbst & van Dishoeck 2009) are readily detected in cores at the prestellar stage (e.g., Bacmann et al. 2012; Jiménez-Serra et al. 2016, 2021; Lattanzi et al. 2020; Scibelli & Shirley 2020; Megías et al. 2023), and are also commonly observed around low-mass protostars (e.g., Jørgensen et al. 2016; Yang et al. 2021). In order to follow the trail of chemical complexity in space, the study of the chemistry of VeLLOs is a crucial step to close the gap between pre- and protostellar objects. To date, only Favre et al. (2020) have discovered emission of methanol, the simplest COM, at a distance of ~1000 au of the VeLLO in L1521F. A search for additional COMs in that source has not been successful to date, due to a lack of sensitivity. To complete our understanding of the complex chemistry that is occurring in these types of objects, more VeLLOs such as L1521F need to be studied in detail.

The study of these young objects is also important in terms of understanding the composition of forming planets. Substructures in the dust of more evolved Class II objects have been linked to the formation of gas giant planets (e.g., Andrews et al. 2018; van der Marel et al. 2019), but signs of ongoing planet formation such as rings and gaps have already been detected in a system with an age of ~500 kyr (Segura-Cox et al. 2020), and most recently Maureira et al. (2024) have reported evidence for annular substructures in a Class 0 source, which suggests that planets can already form earlier in the protostellar evolution (Tychoniec et al. 2020). The composition of planets is set by the composition of the gas and solids they are accreting, and thus the presence of molecules at their location in the disk. The temperature determines which molecules are confined to the solid phase, and which molecules are present in the gas interior to their snowlines (Minissale et al. 2022; Ligterink & Minissale 2023). A change in the temperature, for instance due to an outburst, can temporarily change the composition of the gas due to the shifting

of the snowlines and the associated sublimation of icy species, and by the formation of new gas-phase molecules induced by the species sublimating from the ice. The chemical response time (for e.g., freeze-out) is slower than the shift of physical conditions from the outburst to the quiescent stage. The duration between outbursting events can be estimated from observations and is ~5000–50 000 yr (Scholz et al. 2013; Hsieh et al. 2019). However, most observational tracers that are enhanced due to the outburst remain altered for only ~10–100 yr into the quiescent phase (Zwicky et al. 2024), with exceptions being, for example, CO, which can stay enhanced for up to 10^4 yr before it has frozen out again at typical envelope densities (Visser et al. 2015; Frimann et al. 2017). The emission of the freshly sublimated molecules is expected to be brighter and farther extended than if the object would be quiescent, which makes them easier to detect. Another possibility is to look for species whose formation can be attributed to chemistry that has occurred due to the outburst, and that remain present in the gas phase throughout the quiescent phase.

The aim of this study is to search for signposts of active chemistry that have been induced by the change of physical conditions in the VeLLO in the DC3272+18 cloud during its most recent outburst. The detection of NO for the first time in a source of this type is potentially directly tied to the outburst, and it is proposed that it could act as a tracer of the water snowline in outbursting sources. In addition, this work utilizes molecular tracers for different components to gain a better understanding of the structure of the system.

This paper is structured as follows: the targeted object and the observations are described in Section 2. The detected lines and their analysis are detailed in Section 3 and discussed in Section 4. The conclusions are stated in Section 5.

2. Observations

2.1. Targeted VeLLO in DC3272+18

This study investigates the chemistry toward the isolated VeLLO in the DC3272+18 region, which is located at a distance of 250 ± 50 pc (Kim et al. 2019). There are no massive stars nearby, so external irradiation influences are minimal for this object. The VeLLO has an internal luminosity (L_{int}) of $0.04 \pm 0.02\,L_\odot$, and an envelope mass (M_{env}) of $0.04 \pm 0.08\,M_\odot$ (Hsieh et al. 2018; Kim et al. 2019). Its bolometric luminosity (L_{bol}) of $0.06 \pm 0.01\,L_\odot$ and its bolometric temperature (T_{bol}) of 105 ± 3 K classify it as a late Class 0 object (Dunham et al. 2008; Enoch et al. 2009; Hsieh et al. 2018; Kim et al. 2019). Observations with the Atacama Submillimeter Experiment (ASTE) have found proof of an outflow in the $J = 3-2$ transitions of ^{12}CO, ^{13}CO, and $C^{18}O$, showing blue-shifted asymmetries and wings in the line profiles, mapping of an area of $120'' \times 140''$ with the same facility has revealed outflow lobes as well (Kim et al. 2019). The physical properties of the outflow, such as its dynamical time, were quantified from the bipolarity of the outflow and used to infer a current accretion rate from the outflow, $\dot{M}_{acc}$, of $0.09 \pm 0.01 \times 10^{-6}\,M_\odot\,yr^{-1}$ (Kim et al. 2019). Over the estimated dynamical time of the outflow, the VeLLO will be able to accrete $0.02 \pm 0.01\,M_\odot$, which classifies it as a proto-brown dwarf according to Kim et al. (2019). The emission of the $J = 3-2$ transition of ^{13}CO peaks at a distance of $2.4''$ from the continuum emission peak, which is likely due to the outflow reported in Kim et al. (2019). Observations with the Atacama Large Millimeter/submillimeter Array (ALMA) presented in Hsieh et al. (2018) have inferred from maps of ^{13}CO, $C^{18}O$, and N_2H^+ that

the VeLLO in DC3272+18 has recently undergone an outburst. The observations reveal that the center is devoid of N_2H^+ emission where CO evaporates, because gaseous CO destroys N_2H^+ via the reaction $N_2H^+ + CO \longrightarrow HCO^+ + N_2$. Thus, the location of the N_2H^+ emission can be used to infer the snowline of CO, the location where it freezes out onto the grains. Chemical models by Hsieh et al. (2018) have shown that the CO sublimation radius at $T = 20$ K should be located at 102–164 au, based on its current internal and bolometric luminosity. However, the current sublimation radius of CO is found to be at a distance of 275–311 au. Moreover, the peak of the N_2H^+ emission is located at a distance of 775–1149 au. This is further evidence that the VeLLO has undergone a recent outburst, which has moved the CO snowline outward, closer to the current peak abundance position of N_2H^+ (Hsieh et al. 2018). The study of Hsieh et al. (2018) also conducted modeling in order to constrain the outburst luminosity that is required to lead to the peak position of N_2H^+ and concluded that it can be explained if L_{burst} was 1–4 $L_\odot$, leading to a mass accretion rate of $6 \pm 4 \times 10^{-6} M_\odot yr^{-1}$. This is one order of magnitude higher than what is derived from the outflow by Kim et al. (2019). The models of Hsieh et al. (2018) put the CO sublimation radius during the outburst at a distance of 633–836 au.

2.2. APEX observations

Single-pointing observations with the Atacama Pathfinder EXperiment (APEX) were centered on the VeLLO in the DC3272+18 cloud ($\alpha_{2000} = 15^h42^m16^s.99$, $\delta_{2000} = -52°48'02''.2$) with the nFLASH230 instrument (project-ID O-0109.F-9305A-2022, PI: N. F. W. Ligterink). Two spectral settings were centered on frequencies of 219.6 and 254.4 GHz. The FFTS spectrometer was used as the backend, which provided a bandwidth of 32 GHz observed across $8\times65\,536$ channels with a spectral resolution of 61 kHz (0.07–0.08 km s^{-1}). This resulted in spectral windows of 213.6–221.6 GHz and 229.6–237.6 GHz for setup 1, and 248.4–256.4 GHz and 264.4–272.4 GHz for setup 2. The observations were conducted on April 21–22 and April 28 – May 1 2022 with a precipitable water vapor (pwv) between 0.6 and 1.8 mm. Inspection of the data revealed the presence of prominent atmospheric features, but at frequencies that do not concern the transitions discussed in this work, the meteorological data point toward somewhat unstable conditions during the observations. The typical noise range of the observations is 3–10 mK (rms) for velocity resolutions of 0.07–0.08 km s^{-1}. An outlier is a noise of 140 mK for the CO line at 230.538 GHz (Section 3.2.3). Typical system temperatures during the observations ranged from 76 to 152 K. The main beam efficiency (η_{mb}) for observations at 230 GHz is listed by the APEX website[1] as 0.81, and the half power beam width (HPBW) as 26.2″ for April and May 2022. The observations were conducted in wobbler-switching mode during the first observing session. However, the wobbler position showed contamination of the CO $J = 2-1$ transition at 230.538 GHz from the off position, as the off position was not emission-free from CO. The remaining observations were carried out in position-switching mode with the off position at $\alpha_{2000} = 15^h37^m00^s$, $\delta_{2000} = -51°10'00''$. Thus, observations of the CO line from April 21 were not taken into account for the data analysis. For all other lines, the wobbler-switched and position-switched data were examined, found to be free from contamination from the wobbler-switched off positions, and thus

considered for the data analysis. Dedicated calibration uncertainties for nFLASH230 are not published, thus the calibration uncertainties of 10% as published for the previous APEX-1 and APEX-2 receivers (Dumke & Mac-Auliffe 2010) are assumed. Adopting a distance of 250 pc (Kim et al. 2019) to the source and at the beam size of 26.2″, the observations probe spatial scales of 6550 au in DC3272+18.

3. Results

3.1. Detected molecules

Line identification and baseline fitting were carried out with the CLASS package of the GILDAS[2] software. Line lists were taken from the Jet Propulsion Laboratory (JPL) catalog (Pickett et al. 1998), and the Cologne Database for Molecular Spectroscopy (CDMS; Müller et al. 2005; Endres et al. 2016), the references to the spectroscopic parameters of the molecules that were fit in this work can be found in the Appendix in Table C.2. Identified spectral lines were then fitted with a Gaussian profile with the same program that calculates the peak temperature (T_{peak}), the noise (T_{rms}), the line width (δv), and the line velocity (v_{lsr}). The securely and tentatively detected transitions and the results of the Gaussian fits are listed in Table A.1, their spectra are shown in the appendix (Figs. A.1, A.2). Calibration errors are assumed to be 10% (Section 2.2), thus the uncertainty of the peak intensities is derived as $\sqrt{(0.1T_{peak})^2 + (T_{rms})^2}$. If the T_{peak} of a line is $\geq 3\times$ rms, the line is identified as a detection, if it is $\sim 3\times$ rms, it is identified as a tentative detection. The rms is calculated with the baseline routine in CLASS, Gaussian profiles were fit with CLASS and the CURVE_FIT package of SCIPY (Virtanen et al. 2020).

Most of the detected molecules (Table A.1) are species that are commonly found around protostars. CO, and its ^{13}C- and ^{18}O- isotopologues are securely detected, its minor isotopologue of ^{13}C^{17}O is not detected (Fig. B.1, Table C.1). Kim et al. (2019) found that CO traces the outflow in this VeLLO; in this case one could expect to detect multiple velocity components. While the CO emission is indeed double-peaked, which can hint that the material traces different velocity components, its line shape is consistent with self-absorption. It is to be noted that CO and also ^{13}CO are optically thick, thus self-absorption can indeed contribute to the observed line shapes. This is supported by the finding that the CO absorption peaks at the systemic velocity of the cloud at ~ -0.1 km/s (Hsieh et al. 2018), and therefore one could conclude that the bulk of the emission traced by our observations stems from the on-source position covering the envelope enshrouding the VeLLO instead of the outflow. Fitting CO with two line components did not lead to a good match. The fit of CO in Fig. A.1 was obtained by masking the region that shows self-absorption between –1.7 and 0.75 km/s, and fitting the line with one component. On the other hand, ^{13}CO can be fit well with two components (Fig. A.1), their respective line widths of 0.8 and 0.5 km/s are slightly broadened compared to the rest of the molecules, which predominantly exhibit line widths between 0.35 and 0.5 km/s. This can be seen as a hint that some of ^{13}CO that is observed stems from the outflow reported in Kim et al. (2019), which would explain the broader line widths. Alternatively, this could also be due to the lines being optically thick. The $J = 3-2$ transitions of HCO$^+$, HCN, and HNC, are also securely detected. Moreover, species that are commonly found in UV-irradiated cavity walls carved out by the outflow (Tychoniec et al. 2021), such as c-C$_3$H$_2$ are detected. SO$_2$, a

---

[1] https://www.apex-telescope.org/telescope/efficiency/?yearBy=2022

[2] http://www.iram.fr/IRAMFR/GILDAS

species that is associated with shocks, outflows and sublimation products (Tabone et al. 2017), is securely detected in one transition, and tentatively detected in a second transition. In addition, H_2CO (formaldehyde), CH_3OH (methanol) and SO are detected toward the VeLLO. Deuterated molecules, namely DCO^+, DCN, N_2D^+, one line of D_2CO, and C_2D are found as well. The latter is also a tracer of the cavity walls. Two CH_2DOH lines with favorable upper state energies (<25 K) and Einstein A coefficients ($\sim10^{-5}$ s^{-1}) are below the detection threshold for a tentative detection (Fig. B.1, Table C.1). This is also true for the $H_2^{13}CO$ transition at 219.909 GHz. H_2CO, CH_3OH and SO are species that are typically associated with the emission of warm gas close to a protostar or in the envelope or from both components (e.g., Ceccarelli et al. 2007; Tychoniec et al. 2021). However, the upper energies of the securely detected lines are ~20–44 K. Other H_2CO, CH_3OH and SO transitions covered by the observations with $E_{up} \sim 50$–90 K are not detected. This points toward their origin from the cold, extended envelope. With the exception of CO and ^{13}CO that show multiple line components, the detected molecules have line widths of ~0.35–0.50 km/s, and there is no clear trend that can attribute different molecules to different structures of the system based on their line widths and the v_{lsr} of the different lines. All of the so far mentioned species are routinely observed toward protostars, but the molecular inventory probed by the APEX observations also reveals multiple transitions of nitric oxide (NO) at an intensity of 3–17× rms, and line widths of ~0.4 km/s in the VeLLO, which adds this source to the small list of objects with reported NO detections in the literature (Section 3.3).

The SiO $J = 5_0$–4_0 transition is targeted in the observations, but not detected (Fig. B.1). SiO is a species that is commonly associated with shocks, but the transition at 217.1050 GHz (E_{up} = 31.3 K, A_{ij} = 5.2×10^{-4} s^{-1}; Fig. B.1) is not detected in the spectrum. This could well be due to beam dilution effects, as SiO is a tracer of shocked regions that are more compact (Tychoniec et al. 2021). It is also to note that no species with a higher degree of chemical complexity than methanol are detected in the data. This is also true for species with upper level energies that point toward an origin in the hot gas in close proximity to the VeLLO. This does not rule out their presence, it could also be that the low spatial resolution of the data is not sufficient to detect them due to beam dilution. The highest upper energy for a transition with a secure detection is 48 K, tentative detections have upper level energies of 41–131 K (Table A.1).

3.2. Constraints on the excitation temperature and column density

Subsequent analysis of the detected lines to determine their excitation temperatures and column densities was carried out under the assumption of local thermal equilibrium (LTE). It is assumed that the beam size equals the source size and that both distributions are Gaussian, which leads to a beam filling factor of 0.5. This choice is made based on the assumption that the envelope material fills the beam. The beam-filling factor affects the column density, but as the detected lines are mainly optically thin, the derived column densities would be scaled by the beam-filling factor. If the molecules emit from the same region, the abundance ratios are independent of the choice of filling factor.

3.2.1. Rotational diagram analysis of c-C_3H_2

Under the assumption that LTE is applicable, the distribution of the molecular energy levels follows a Boltzmann distribution, and the upper state level population (N_u) divided by the statistical weight (g_u) of the molecular energy levels can be related to their upper level energies (E_u) by the Boltzmann equation:

$$\frac{N_u}{g_u} = \frac{N_{tot}}{Q(T_{rot})} e^{-E_u/kT_{rot}} \tag{1}$$

where k is the Boltzmann constant, N_{tot} is the total column density, and Q corresponds to the partition function value at the corresponding rotational temperature, T_{rot}. In a conventional rotational diagram analysis (e.g., Blake et al. 1987; Goldsmith & Langer 1999), taking the logarithm of Eq. (1) allows for a linear least squares regression:

$$\ln\frac{N_u}{g_u} = \ln N_{tot} - \ln Q(T_{rot}) - \frac{E_u}{kT_{rot}}. \tag{2}$$

In LTE, the rotational temperature T_{rot} corresponds to the excitation temperature T_{ex}. By constructing a semi-log plot of N_u / g_u against E_u, the rotational temperature, T_{rot}, and the total column density, N_{tot}, can be derived from the best-fit slope and intercept, respectively. As the optical depth of the transitions is unknown, an optical depth correction factor, C_τ, needs to be applied, to account for cases in that the optical depth is $\tau \ll 1$

$$C_\tau = \frac{\tau}{1 - e^{-\tau}}. \tag{3}$$

Therefore, the right-hand side of Eq. (2) is rewritten as:

$$\ln(N_{tot}) - \ln Q(T_{rot}) - \ln C_\tau - \frac{E_u}{kT_{rot}}. \tag{4}$$

The optical depth of each transition is calculated via

$$\tau_{ul} = \frac{A_{ul}c^3}{8\pi\nu^3\delta v} N_u(e^{\frac{h\nu}{kT_{rot}}} - 1). \tag{5}$$

The A_{ul} corresponds to the Einstein A coefficient, c to the speed of light, ν to the frequency, and δv to the line width. This allows to rewrite C_τ as a function of N_u, and substitute it into Eq. (4) to construct a likelihood function $\mathcal{L}(N_u, T_{rot})$ for χ^2 minimization. This likelihood function is used with the affine-invariant Markov Chain Monte Carlo (MCMC) code `emcee` (Foreman-Mackey et al. 2013) to determine N_u and T_{rot}.

This method requires multiple transitions per molecule to ensure a meaningful fit, thus this method is only applied to c-C_3H_2. The result is obtained with two calculations. First, a broad parameter space for the total column density N_{tot} = 10^7–10^{14} cm^{-2} and T_{rot} = 10–500 K is explored with 50 walkers and 500 steps. Those results are used to narrow down the parameter space to N_{tot} = 10^{11}–10^{13} cm^{-2} and T_{rot} = 10–100 K. After 2000 steps with 50 walkers, a column density of N_{tot} = $3.78^{+0.37}_{-0.40} \times 10^{11}$ cm^{-2} and a T_{rot} of $35.4^{+3.2}_{-4.9}$ K are obtained. Parameters and uncertainties correspond to the 50th, 16th, and 84th percentiles from the marginalized posterior distributions. The resulting population diagram is plotted in Fig. 1 and reveals that c-C_3H_2 traces a warm gas component in the VeLLO in DC3272+18. This species is commonly associated with the cavities carved by protostellar outflows (e.g., Murillo et al. 2018; Tychoniec et al. 2021), and it is likely that it indeed traces the cavities of the outflow that Kim et al. (2019) have detected in CO. The opacities of the c-C_3H_2 transitions are in the range of 0.002–0.006.
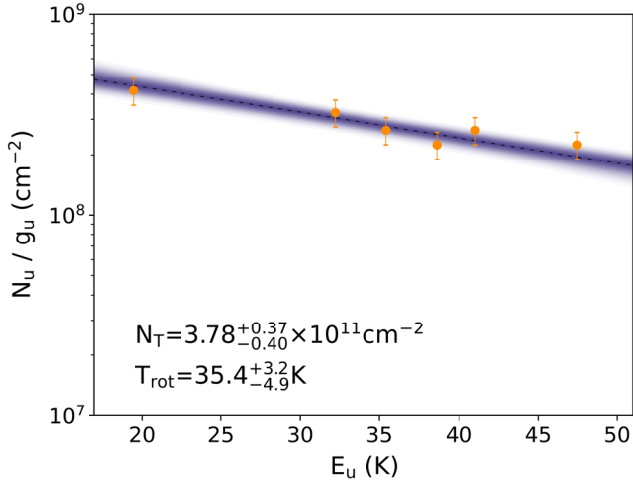
Fig. 1. Population diagram for c-C_3H_2. The shaded region in purple marks the region between the 16th and 84th percentile. Here, N_T corresponds to the total column density.

Table 1. Column densities for the detected species.

Species	N_{obs} (10^{11} cm^{-2}) $T_{ex} = 10$ K	$T_{ex} = 30$ K	$T_{ex} = 50$ K
HCN	$3.02^{+0.53}_{-0.51}$	$1.51^{+0.25}_{-0.22}$	$1.74^{+0.29}_{-0.30}$
DCN	$0.51^{+0.06}_{-0.08}$	$0.36^{+0.05}_{-0.04}$	$0.44^{+0.06}_{-0.07}$
HCO$^+$	$18.62^{+3.26}_{-2.77}$	$7.59^{+0.83}_{-0.93}$	$8.71^{+0.95}_{-1.07}$
DCO$^+$	$4.27^{+1.23}_{-1.25}$	$2.75^{+0.76}_{-0.79}$	$3.47^{+0.96}_{-0.90}$
HNC	$18.20^{+1.30}_{1.60}$	$7.59^{+0.51}_{-0.73}$	$8.71^{+0.58}_{-0.62}$
N$_2$D$^+$	$1.32^{+0.34}_{-0.32}$	$0.83^{+0.22}_{-0.20}$	$0.10^{+0.03}_{-0.02}$
NO	$1000.00^{+96.48}_{-160.11}$	$707.95^{+86.38}_{-76.99}$	$912.01^{+111.28}_{-99.18}$
D$_2$CO	$0.79^{+0.22}_{-0.20}$	$0.54^{+0.15}_{-0.14}$	$0.79^{+0.22}_{-0.21}$
SO	$32.73^{+7.54}_{-7.90}$	$8.51^{+0.28}_{-0.28}$	$8.41^{+0.32}_{-0.31}$
C$_2$D	$4.67^{+1.05}_{-1.08}$	$3.24^{+0.72}_{-0.75}$	$4.07^{+0.91}_{-0.94}$
CH$_3$OH	$97.72^{+28.48}_{-31.14}$	-	-
H$_2$CO	$20.95^{+3.61}_{-3.74}$	-	-

Notes. The column densities were derived via the grid-fitting method for T_{ex} of 10, 30, and 50 K with the exception of CH$_3$OH and H$_2$CO, where only the values calculated at 10 K are shown (see text for discussion).

3.2.2. Constraining the excitation temperature of methanol and formaldehyde

Methanol and formaldehyde emit from a cold gas reservoir in the envelope surrounding the VeLLO. In DC3272+18 one H$_2$CO transition at 218.2222 GHz with an upper level energy of 20.96 K is detected (Fig. A.1). However, two additional transitions at 218.4756 GHz ($J = 3_{2,2}-2_{2,1}$) and 218.7601 GHz ($J = 3_{2,1}-2_{2,0}$), both with E_{up} of 68.1 K, are not detected. Assuming that intensities >3× rms correspond to a detection, an LTE model that is based on the formalism of the CASSIS[3] (Vastel et al. 2015) software was utilized to explore column densities in combination with excitation temperatures of 10–50 K in 5 K steps that simultaneously match the T_{peak} value of the detection at 218.222 GHz and the non-detection of the two other transitions. First, the fixed excitation temperature was used to find a column density that can reproduce the line intensity of the observed H$_2$CO transition. In a second step, this column density and excitation temperature was used to obtain the peak intensity of the two other H$_2$CO transition. Only at $T_{ex} = 10$ K the two other transitions remain undetected.

This was also tested for 12 additional transitions of CH$_3$OH with E_{up} in the range of ~50–90 K in addition to the two lines that are detected in DC3272+18. As for H$_2$CO, it was not possible to reproduce the detected lines without overproducing the intensities of the non-detections at $T_{ex} > 10$ K. Thus, the H$_2$CO and CH$_3$OH detected in the APEX data stem from a cold gas component and not from a potential hot corino, which are regions close to the protostar that have $T > 100$ K and are thus associated with the sublimation of COMs (Ceccarelli et al. 2007). If a second, warmer gas reservoir is present, the spatial resolution of the observations is not sufficient to detect this emission.

3.2.3. Grid-fitting of species tracing the cold gas

Species such as N$_2$D$^+$, HNC, HCN, DCN, HCO$^+$, and DCO$^+$ are commonly associated with the cold envelope (e.g., Tychoniec et al. 2021), and thus likely emit from a region with conditions similar to H$_2$CO and CH$_3$OH. In order to determine

the column densities of these species, the excitation temperature is set to a fixed value of 10 K, which corresponds to T_{ex} derived from H$_2$CO and CH$_3$OH, but it is also the value used by Hsieh et al. (2018) to fit the column densities of N$_2$H$^+$ and the CO isotopologues. CASSIS is used to fit over a grid of N_{tot} assuming LTE conditions. The position of the lines is set to the source v_{LSR} of –0.1 km/s, the full width half maximum (FWHM) are set to the values given in Table A.1, and the source size is set to match the beam size. Model spectra are computed with a step size of 0.01 in logarithmic space to explore column densities in the range of 10^{10}–10^{15} cm^{-2}. The best-fit column densities and their 2σ uncertainties for each of the above-mentioned molecules, as well as NO, SO, and D$_2$CO are listed in Table 1. CO and its isotopologues were excluded from this process. CO and ^{13}CO do suffer from optical depth issues. C^{18}O is potentially affected as well, while the rms at the position of the covered ^{13}C^{17}O transition is only ~2× rms, and therefore counted as a non-detection. Optical depth is not an issue for the remaining molecules, as τ is found to be < 1.

3.3. Detection of NO

Seven transitions of NO (six secure, one tentative) are detected around the DC3272+18 VeLLO, which adds it to a small list of different types of sources that have reported detections of this molecule. It has been detected in the dark clouds TMC-1 and L134N (McGonagle et al. 1990; Gerin et al. 1993), around the low-mass protostars NGC 1333 IRAS 4A, SVS13-A, and IRAS 16293–2422 B, in the shock of L1157-B1 (Yıldız et al. 2013; Codella et al. 2018; Ligterink et al. 2018), in the high-mass star-forming region Sgr B2 toward Sgr B2(M) and Sgr B2(N) (Liszt & Turner 1978; Ziurys et al. 1994; Halfen et al. 2001), and most recently in the dust trap of the Oph-IRS 48 disk (Brunken et al. 2022; Leemker et al. 2023). For Oph-IRS 48, models have shown that its abundance can be increased when ice sublimation boosts the abundance of H$_2$O and NH$_3$ (Leemker et al. 2023). The main formation pathway of NO is the gas-phase neutral-neutral reaction

$$N + OH \longrightarrow NO + H \qquad (6)$$

---

[3] http://cassis.irap.omp.eu/

in oxygen-enriched gas, where OH is a product of the photodissociation of water.

It can also form via a second neutral-neutral reaction, namely

$$NH + O \longrightarrow NO + H \tag{7}$$

([Millar et al. 1991](); [Baulch et al. 2005](); [Wakelam et al. 2012]()). In addition, photodissociation of species such as HNO, N_2O, and NO_2 can also produce NO ([van Dishoeck et al. 2006](); [Heays et al. 2017]()), but these species are usually neither abundant nor commonly detected around protostars, so their contribution to the abundance of NO is presumably small. After its formation NO can deplete from the gas by accreting onto dust grains, where it gets hydrogenated to form species such as NH_2OH ([Congiu et al. 2012](); [Fedoseev et al. 2012]()). The formation of N_2O is a by-product of the hydrogenation process of NO to NH_2OH. A ratio <1 for NO/N_2O would indicate that some of the NO is lost to this formation channel. However, the observed frequency range only covers one N_2O transition at 251.2216 GHz that is not detected, likely due to its high E_{up} (63.3 K) and low A_{ij} coefficient (2.3×10^{-6} s^{-1}), so it is not possible to assess whether some NO has already been frozen out and has been incorporated in grain surface processes via this pathway. If returned back into the gas phase, the photodissociation of NH_2OH can also form NO, but this destruction channel is not efficient ([Gericke et al. 1994](); [Fedoseev et al. 2016]()). The predominant product channel from photodissociated NH_2OH leads to NH_2 + OH, which is not a direct parent species for NO ([Betts & Back 1965]()). In addition to freezing out, NO can be directly destroyed in the gas phase via photodissociation reactions, or the reaction N + NO $\longrightarrow N_2$ + O ([Millar et al. 1991]()). However, photodissociation induced by internal UV photons from the VeLLO during its quiescent phase is less effective than during the outburst, so while increased UV flux during the outburst can indeed boost the photodissociation of species such as H_2O and NH_3, which would deliver the reactants to form NO from the two neutral-neutral reactions in Eq. (6) and (7), the photodissociation of NO after the VeLLO has returned to its quiescent phase does play a smaller role. NO has a low binding energy ($\sim$1600 K; [Wakelam et al. 2017]()), and thus does not freeze out rapidly after the gas in the envelope cools down to its pre-outburst temperature. The sublimation temperature of NO is $\sim$30–50 K, so in current envelope conditions its presence in the gas phase cannot be explained by thermal desorption. In addition, internal UV photons from the quiescent VeLLO do not lead to significant photodissociation, while its isolated position in the DC3272+18 region distances it from external UV flux. On the other hand, H_2O has a binding energy of $\sim$5640 K, which requires temperatures between 90 and 140 K in the interstellar medium (ISM) to sublimate, and already freezes out after 10^2–10^3 yr at typical envelope densities ([Minissale et al. 2022]()).

As for the other species, the beam size of the observations does not allow the location of the NO emission to be spatially resolved. Under the assumption that the molecular emission is co-spatial, the column density of NO is for example 10 times higher than that of CH_3OH, which is a species that freezes out on similar time scales as water (e.g., [Collings et al. 2004]()), so this indicates that the freeze-out process of NO has not progressed as far as it has for instance for CH_3OH, yet.

3.4. D/H ratios

The average ratio of deuterium over hydrogen (D/H ratio) in the local ISM is $\sim 2 \times 10^{-5}$ ([Linsky et al. 2006](); [Prodanović et al.

Table 2. D/H ratios calculated with a fixed T_{ex} of 10 K.

Ratio	D/H ratio w. stat. corr.
DCO^+/HCO^+	$0.23^{+0.10}_{-0.11}$
DCN/HCN	0.17 ± 0.05
D_2CO / H_2CO	0.19 ± 0.04

2010). Molecules with an enrichment in deuterium by up to 4 orders of magnitude compared to the interstellar average are often linked to a formation before the protostellar stage, as temperatures <20 K boost deuterium fractionation ([Caselli & Ceccarelli 2012]()). The D/H ratios for the deuterated molecules in Table 2 have been calculated based on the column densities in Table 1, but it is to note that all ratios have been derived based on one transition per molecule, and therefore, the presented values should be interpreted with caution. All D/H ratios are in the percent range (17–23%), thus pointing to an origin from a cold environment, potentially before the formation of the VeLLO. DCO^+ and DCN formation occurs in the gas phase ([Willacy 2007]()), while D_2CO forms via grain-surface reactions at temperatures < 20 K ([Nagaoka et al. 2007](); [Hidaka et al. 2009]()). The derived D/H ratios in the VeLLO are comparable to findings in prestellar cores and around low-mass protostars ([Bizzocchi et al. 2014](); [Chacón-Tanarro et al. 2019](); [Ambrose et al. 2021](); [Drozdovskaya et al. 2022](); [Lin et al. 2023]()) and thus favor their prestellar origin and subsequent inheritance to the protostellar stage.

3.5. Physical conditions implied by line intensity ratios

The line intensity ratios of emission lines can be utilized to probe the physical conditions in the ISM. [Hacar et al. (2020)]() demonstrated that the intensity ratio of the $J = 1-0$ transitions of HCN and HNC can be used to infer the kinetic gas temperature and derived a two-component scaling relation from large-scale observations in Orion. This scaling relation is attributed to different HNC destruction pathways whose efficiency depends on the temperature. [Hacar et al. (2020)]() deduce the scaling relation from the $J = 1-0$ transitions of HCN and HNC. As a test in this work, it is assumed that the relation also holds true for the $J = 3 - 2$ transitions that are detected in DC3272+18. The peak intensities listed in Table A.1 assume a flux calibration uncertainty of 10%. However, both HCN and HNC are observed in the same sideband, thus a relative calibration uncertainty within the band of 1% is assumed, resulting in an error of $\sqrt{(0.01 T_{peak})^2 + (T_{rms})^2}$. The line intensity ratio I_{HCN}/I_{HNC} derived from the T_{peak} values in DC3272+18 is 0.27 ± 0.07. Thus, the scaling relation for $I_{HCN}/I_{HNC} < 4$ given in Eq. 3 in [Hacar et al. (2020)]() would apply, which yields T_{kin} (K) $= 10 \times I_{HCN}/I_{HNC} = 2.68 \pm 0.7$ K, which would put the kinetic temperature below the cosmic background temperature if this scaling law holds true. However, [Hacar et al. (2020)]() point out that this relation is only valid down to kinetic temperatures of 15 K, below the errors become large, for example errors in T_{kin} are >5 K for intensity ratios <1. Therefore, this method cannot be used to derive the kinetic temperature, but it reveals that it must be cold, likely below the 15 K threshold, where the scaling law is not valid anymore. This is also supported by additional line ratios that offer tighter constraints.

[Murillo et al. (2018)]() conducted a survey of twelve low-mass protostellar systems in Perseus with APEX. The frequency range

of their observations partially overlaps with the range observed in this work, thus the line intensity ratios of the two works can be compared. The first intensity ratio that is considered is $I_{\mathrm{DCN}}/I_{\mathrm{DCO^+}}$. This is due to the D/H ratio of both molecules, which is tied to chemical pathways leading to their deuteration at different temperatures. Both transitions discussed here were observed in the same sideband, thus a flux calibration uncertainty of 1% is assumed. This ratio can be used as a proxy for the gas temperature. While $\sim 2 \times 10^{-5}$ corresponds to the average D/H ratio in the local ISM (Linsky et al. 2006; Prodanović et al. 2010), species get enriched in deuterium when the deuterium fractionation becomes efficient once temperatures drop below 20 K and gas densities reach $10^4\,\mathrm{cm^{-3}}$ via the reaction

$$H_3^+ + HD \rightleftharpoons H_2D^+ + H_2 + \Delta E, \tag{8}$$
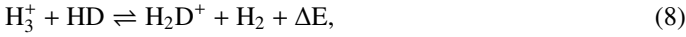
where $\Delta E = 232\,\mathrm{K}$ (Watson 1974). DCO^+ subsequently forms from the reaction of $H_2D^+ + CO$, thus it has been deemed a suitable tracer for the cold gas (Jørgensen et al. 2005; Murillo et al. 2015). Then, DCO^+ can propagate its deuteration to DCN (Willacy 2007) via
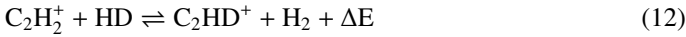
$$DCO^+ + HNC \longrightarrow HNCD^+ + CO \tag{9}$$

and

$$HNCD^+ + e^- \longrightarrow DCN + H. \tag{10}$$

Once the temperature increases to $>30\,\mathrm{K}$, a second pathway leading to deuteration fractionation starts to dominate, namely via the reactions

$$CH_3^+ + HD \rightleftharpoons CH_2D^+ + H_2 + \Delta E \tag{11}$$

and

$$C_2H_2^+ + HD \rightleftharpoons C_2HD^+ + H_2 + \Delta E \tag{12}$$

(Millar et al. 1989; Roueff & Lique 2013), where ΔE is $\sim 390\,\mathrm{K}$ for the first reaction (Asvany et al. 2004), and $\sim 550\,\mathrm{K}$ for the second reaction (Herbst et al. 1987).

CH_2D^+ is the starting point for DCO^+ (via $CH_2D^+ + CO \longrightarrow DCO^+ + CH_2$; Favre et al. 2015) and DCN formation (via $CH_2D^+ + e^- \longrightarrow CHD + H$ followed by $CHD + N \longrightarrow DCN + H$; Millar et al. 1989). Both routes are most efficient for temperatures of $\sim 70–100\,\mathrm{K}$ (Favre et al. 2015). The intensity ratio of $I_{\mathrm{DCN}}/I_{\mathrm{DCO^+}}$ in DC3272+18 is 0.050 ± 0.005, which is lower by a factor of ≥ 2 than the values that Murillo et al. (2018) derive for their sample of low-mass protostars. The low intensity of DCN does not suggest significant contribution from the warm formation pathway. It is also most likely that DCO^+ forms solely from the cold formation pathway, and has not proceeded to form a substantial amount of DCN, yet. Thus, the combination of the low value derived for $I_{\mathrm{HCN}}/I_{\mathrm{HNC}}$ and the high intensity of DCO^+ strongly hints that the probed material around the VeLLO is predominately cold.

This is also concluded from two additional sets of line ratios that are calculated to probe the gas temperature from c-C_3H_2 transitions. The $6_{0,6}–5_{1,5}$ and $3_{3,0}–2_{2,1}$ transitions of c-C_3H_2 have E_{up} of 38.6 and 19.5 K, respectively, thus their intensity ratio can give hints about the gas temperature, too. This also applies to the ratio of the $5_{1,4}–4_{2,3}$ transition ($E_{\mathrm{up}} = 35.4\,\mathrm{K}$) over the $3_{3,0}–2_{2,1}$ ($E_{\mathrm{up}} = 19.5\,\mathrm{K}$) transition. As for the other two ratios discussed above, all transitions were observed in the same sideband, a flux uncertainty of 1% is therefore assumed. The derived intensity ratios are 0.297 ± 0.040, and 0.173 ± 0.014, respectively, which yet again indicates that the warmer transitions are less excited
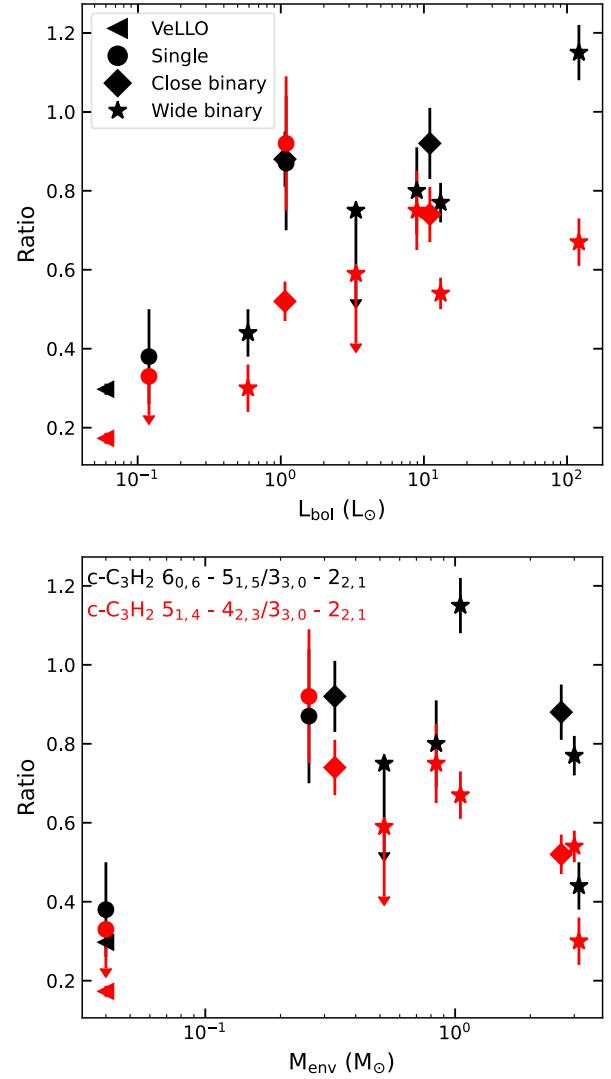

Fig. 2. Line intensity ratios of c-C_3H_2 transitions for the VeLLO, and the sample of Murillo et al. (2018) that consists of single protostars, close binary systems, and wide binaries. Close binaries in Murillo et al. (2018) are separated by $<2''$, the wide binaries in this work have separations in the range of $7–46''$. The ratios are plotted against the bolometric luminosity, L_{bol} in the upper panel, and against the envelope mass, M_{env} in the lower panel.

as the gas probed by the observations is cold. The line ratios obtained for the VeLLO are also on the lower end of the range of ratios that Murillo et al. (2018) derive for their sample of low-mass protostars, which are $\sim 0.38–1.15$ and $0.3–0.92$ for the two c-C_3H_2 ratios, respectively. The ratios do not seem to depend on the mass of the envelope, but they do scale with the bolometric luminosity (Fig. 2), as lower ratios are found for the faintest sources.

Thus, even though it is not possible with the current data to derive an exact value for the excitation temperature of the detected molecules, the line intensity ratios also strongly suggest that the probed material is predominantly cold. The low ratio of $I_{\mathrm{DCN}}/I_{\mathrm{DCO^+}}$ suggests a kinetic gas temperature of $<30\,\mathrm{K}$, as otherwise DCN should be more abundant, and the ratio of $I_{\mathrm{HCN}}/I_{\mathrm{HNC}}$ suggests an even lower value of $\leq 15\,\mathrm{K}$. These findings are in line with the excitation temperature that was derived for formaldehyde and methanol (Section 3.2.2).

3.6. Line emission and system parameters

The large beam of the observations (26.2″) does not allow different physical components of the system to be resolved. However, the variety of the detected species and specifically their detected transitions can constrain the physical conditions and structures around the VeLLO. The discussed line ratios in Section 3.5, and the constraint on T_{ex} of 10 K for species such as H_2CO and CH_3OH imply that most of the gas around the VeLLO is cold. This is supported by the detection of molecular tracers that are commonly associated with the cold envelope, such as DCO^+ and N_2D^+ (Tychoniec et al. 2021). In addition to their excitation temperature, their narrow line width of ~0.5 km/s points to its origin from the cold envelope as well. This is also likely for the species NO, SO, H_2CO, and CH_3OH. In contrast, $c-C_3H_2$ is a molecule commonly associated with the cavity walls carved out by the outflow. This is strongly supported by the population diagram fit that derives a rotational temperature of ~35 K for $c-C_3H_2$, indicating that it traces a second, warm gas reservoir around the VeLLO. The presence of an outflow cavity is also supported by the detection of multiple C_2D lines (Tychoniec et al. 2021). SiO is commonly used to trace shocks around protostars, as it is linked to the destruction of Si-rich grains due to the high temperatures induced by shocks. The non-detection of SiO in the DC3272+18 cloud suggests that either no shock is present in this source, or that it is too weak to destroy dust grains. The presence of SO_2 does not clearly support the detection of a shock either. While it can be a tracer of shocked gas, it is also often associated with sublimated grain-surface species (Tychoniec et al. 2021). The $4_{2,2}-3_{1,3}$ transition with an upper energy of 19.0 K is securely detected, and most likely traces the same gas reservoir as species such as NO and CH_3OH, namely the cold envelope. A second SO_2 transition with E_{up} of 130.7 K is only tentatively detected, a warmer gas reservoir, for example one that is heated by a shock, would be necessary to excite this line. However, no other shock tracers such as H_2CO, CO and SO transitions with high E_{up} are detected (Tabone et al. 2020; Tychoniec et al. 2021), so it is unlikely that the APEX observations have picked up signatures of shocked material. In contrast, tracers of the outflow from the VeLLO are detected. Previous observations of Kim et al. (2019) had already confirmed the presence of an outflow in ^{12}CO, ^{13}CO, and $C^{18}O$, and the line widths of those molecules are broadened by ~20% compared to species such as C_2D or CH_3OH in the APEX data.

The here presented observations indicate that the majority of the probed material stems from the cold envelope. Molecular tracers attributed to the outflow, and the cavity walls have also been detected.

4. Discussion

4.1. NO could potentially trace the water snowline

The high column density of NO relative to CH_3OH can be interpreted as a chemical signpost of the past outburst. If NO and methanol indeed probe the same region, with all evidence pointing to it being the cold envelope, their column density ratio at T_{ex} of 10 K comes to ~10 (Table 1). Thus, NO is estimated to be more abundant than CH_3OH by one order of magnitude. This is in contrast to all NO detections that have been reported so far. NO is 1–3 orders of magnitudes less abundant in the low-mass protostars IRAS 16293-2422 B (Jørgensen et al. 2018; Ligterink et al. 2018) and SVS-13A (Bianchi et al. 2017), and the shock in L1157-B1 (Codella et al. 2018). Grain-surface formation of NO and CH_3OH and subsequent thermal sublima-

tion during the quiescent phase can be ruled out. NO has a binding energy of 1600 K and thermally desorbs at ~30–50 K (Collings et al. 2004; Wakelam et al. 2017), CH_3OH has a binding energy of 5500–6600 K, which leads to a desorption temperature of ~100 K (Collings et al. 2004; Sakai & Yamamoto 2013; Minissale et al. 2022). Thus, the current temperature in the envelope would not allow for efficient thermal desorption of either of the two species. In addition, NO is hydrogenated to form NH_2OH once it freezes out onto the grain surfaces (Fedoseev et al. 2016), therefore it is not likely that abundant NO is sublimated directly from the grain surfaces. It is more likely that the high NO column density is linked to its efficient formation after the outburst in the gas phase. Its main formation pathway in the gas phase (Eq. (6)) requires N and OH. The increased temperature during the heating event leads to the sublimation of icy material containing species such as CH_3OH, but more importantly H_2O and NH_3, which all desorb at temperatures of ~100 K (Collings et al. 2004; Wakelam et al. 2017; Minissale et al. 2022). Photodissociated products of the major ice constituents H_2O and NH_3 (Boogert et al. 2015) are then consumed to form NO at the location where the water snowline got shifted to during the outburst. Due to the increased UV flux from the VeLLO during the outburst the efficiency of photodissociation is elevated, which provides the necessary ingredients to form abundant NO in the gas phase. Thus, the presence of NO at a high column density relative to methanol could be a direct consequence of the outburst of the VeLLO. After the end of the accretion outburst the temperature will decrease again as the VeLLO reaches its quiescent phase. Subsequently, species that have been evaporated during the outburst will start to freeze out again, that order depends on the binding energies of the molecules. Chemical models by Visser et al. (2015) have shown that the water snowline moves outward by a factor of ~10 during the outburst and that H_2O abundances remain enhanced for 10^2–10^3 yr after the outburst. In the case of CO the enhancement is seen for 10^3–10^4 yr, so while it is not possible to pinpoint the exact point in time of the outburst, the extended CO snowline compared to its quiescent luminosity (Hsieh et al. 2018) is evidence that the outburst happened less than 10^4 yr ago. The results presented in this paper show that NO could be another molecule that serves as a tracer that is available for longer timescales than the typical 10^2–10^3 yr of most direct tracers of the water snowline. Its longevity as a tracer is reflected in the elevated NO/CH_3OH ratio. Due to its higher binding energy, CH_3OH starts its freeze-out in a point in time closer to the outburst, while NO still remains in the gas phase. If NO indeed forms from the reaction in Eq. (6), it can be used to expose the location of the position of the shifted water snowline during the outburst, as this proposed formation pathway is tightly linked to species that sublimate/freeze out at the water snowline. This would add NO to the list of tracers of the water snowline that is more commonly probed via HCO^+, CH_3OH, HDO and $H_2^{18}O$ (Hsieh et al. 2019; Tobin et al. 2023). Observations with a better spatial resolution are required to confirm the suspected co-spatial origin of the NO and CH_3OH emission.

4.2. Other mechanisms that could lead to the presence to NO

While an outburst that leads to sublimation of grain-surface species due to its accompanied temperature increase in the envelope followed by boosted photodissociation due to its higher UV flux during its active phase is a possibility to explain the peculiarly high NO abundance in the VeLLO, other options also

need to be considered. Another mechanism that can release grain surface species into the gas phase and that consequently has to be considered as an alternative explanation is reactive desorption. Reactive desorption is a nonthermal desorption process where the energy of chemical reactions on the grains is not fully absorbed by the grain, and the remaining energy causes the ejection of a percentage of the newly formed product in the gas-phase (e.g., Vasyunin et al. 2017; Pantaleone et al. 2020). This process is responsible for the presence of COMs such as CH_3OH in the gas in prestellar cores (e.g., Jiménez-Serra et al. 2016), and could also contribute to the molecular abundances in the envelope around the VeLLO. Chemical models find that 1–10% of the formed grain surface product gets ejected into the gas phase via this desorption process (e.g., Garrod et al. 2008). Thus, reactive desorption processes could have released CH_3OH into the gas phase, which would be an alternative explanation to thermal desorption induced by the outburst. This is also true for H_2O and NH_3. However, without an outburst that increases the internal UV flux and photodissociates H_2O and NH_3 it is unlikely that the reactants required to form NO via Eq. (6) and (7) are abundant enough to result in a column density ratio of ten for NO/CH_3OH.

Another possibility is that the outflow emanating from the VeLLO sublimates grain-surface species locally. Yet again, this option could therefore explain the presence of CH_3OH in the gas. However, there are two caveats coming with this option. First, lines of molecules in the outflow are usually broadened, as it is seen for CO and ^{13}CO, but not for CH_3OH. Second, as for the explanation with reactive desorption, this option does not present an effective path toward photodissociation of H_2O and NH_3. Thus, it is unlikely that the outflow played a major role in the formation of NO, and the presence of gaseous CH_3OH in this source. If it contributes marginally can only be assessed with observations with a higher spatial resolution. If those species are originating from the outflow cavity wall, a shift in their v_{vlsr} would be expected.

Thus, an outburst is the most likely explanation for the high abundance of NO in the VeLLO. However, based on the available data it is not possible to fully rule out other options or a combination of multiple scenarios.

4.3. Limits on Complex organic molecules

COMs are precursors of prebiotic molecules, thus revealing their formation pathways in space is a central interest of astrochemical studies. Around protostars they are often associated with hot cores or hot corinos, which is a region in close proximity to the protostar that has warmed up sufficiently to sublimate COMs from icy grains and form them actively in the gas phase (Ceccarelli et al. 2007; Herbst & van Dishoeck 2009). Nevertheless, they are also readily detected in cold, prestellar cores, where their presence in the gas phase is attributed to nonthermal desorption processes such as reactive desorption (Garrod & Herbst 2006; Vasyunin et al. 2017), or cosmic ray-induced desorption (Sipilä et al. 2021). The most complex species detected in the VeLLO is CH_3OH, the question now becomes whether the VeLLO is COM-poor, or if the current sensitivity is not sufficient to detect more complex species, or if the beam dilution effects hamper the chance of a detection. This has been tested for three COMs that are routinely detected around protostars and in cores, namely methyl formate (CH_3OCHO), dimethyl ether (CH_3OCH_3), and acetaldehyde (CH_3CHO). Their abundance relative to methanol is found to be in the range of 1–40% for low-mass protostars (Jørgensen et al. 2018; Belloche et al. 2020;

Yang et al. 2021). In the well-studied prestellar core L1544, Jiménez-Serra et al. (2016) find an abundance of 2.0–2.5% for dimethyl ether relative to methanol, 5.9–7.4% for methyl formate, and 2.0–8.2% for acetaldehyde for two positions in this core. In addition, Scibelli & Shirley (2020) detect acetaldehyde in 22 prestellar cores, with a ratio of CH_3CHO/CH_3OH of 2–26%. As the majority of the probed material in the VeLLO is cold, and it is likely that potential COM emission from a warm gas component close to the VeLLO will not be detected due to the large beam of the observations, an excitation temperature of 10 K was chosen to test which ratio of COM/CH_3OH would have led to a detection in the APEX data. The rms of the data is typically 3–5 mK (Table A.1), and the same LTE model that was used to constrain the excitation temperature of H_2CO and CH_3OH was used to derive column densities that would lead to T_{peak} intensities of $3 \times$ rms for transitions covered in the data that have E_{up} of ≤ 50 K. In the case of acetaldehyde, a ratio of 30–40% compared to methanol would be required for a detection in the APEX observations. For acetaldeyde and methyl formate this value is >60%. Thus, it is very unlikely that they could have been detected in the current observational data.

5. Conclusions

This work presents APEX observations of the VeLLO in the isolated DC3272+18 cloud that has undergone an outburst that likely occurred less than 10^4 yr ago. The presence of molecules such as CH_3OH, H_2CO, SO, SO_2, and for the first time in a source of this type, NO, is likely tied to the past heating event. Moreover, typical chemical tracers of multiple physical components of the protostellar system are detected. Line intensity ratios and column densities are utilized to constrain the kinetic gas temperature of the system and the excitation temperature of the detected species. The main findings are listed below:

- For the first time, NO is detected in a VeLLO. The most likely explanation for its high column density is its formation after species such as H_2O and NH_3 have been sublimated and subsequently photodissociated after the outburst. If this proposition holds true, it could be used to trace the position of the extended water snowline during the outburst. Due to its high volatility it remains enhanced in the gas phase long after the central object has returned to its quiescent stage. Its potential as a tracer for past outbursts has to be tested with observations with a higher spatial resolution for this source, and for a larger sample of sources as well. This is especially interesting to test for Class I and II objects when planet formation is already an ongoing process.
- The detection of CH_3OH and H_2CO with an excitation temperature of ~10 K suggests that they stem from the cold envelope and have sublimated from the grains during the outburst. The securely detected transitions of SO with $E_{up} < 44$ K most likely originate from the same gas reservoir. The high column density ratio of NO/CH_3OH is attributed to different freeze-out timescales of molecules related to their binding energies. Observations with a higher spatial resolution are required to confirm that those molecules are indeed co-spatial.
- The low line intensity ratio of I_{HCN}/I_{HNC} indicates that the gas kinetic temperature is ≤ 15 K. A low kinetic temperature is also supported by the low line intensity of the I_{DCN}/I_{DCO^+} ratio. When compared with APEX observations of a sample of low-mass protostars in Perseus (Murillo et al. 2018), the ratios of the VeLLO are low compared to the other objects,

in line with its low bolometric luminosity and envelope mass compared to the rest of the sample.

– The detections of c-C$_3$H$_2$ and C$_2$D are consistent with the presence of cavity walls carved out by the outflow driven by the VeLLO. The population diagram analysis of the c-C$_3$H$_2$ transitions calculates a rotational temperature of 35^{+3}_{-5} K, and thus reveals a second, warmer layer of gas around the VeLLO. However, ratios of the 6-5/3-2 and 5-4/3-2 transitions of c-C$_3$H$_2$ are also lower than what is found in the sample by Murillo et al. (2018), so while c-C$_3$H$_2$ traces a reservoir that is warm compared to the rest of the probed material in the VeLLO, it is still colder compared to the material that is found around low-mass protostars.

– The detections of three deuterated species, namely DCO$^+$, DCN, D$_2$CO, and their respective D/H ratios reveal that deuteration has been effective in the past and potentially also in the present. C$_2$D is also detected in the data, but C$_2$H is not covered, so its D/H ratio cannot be calculated. D$_2$CO is a product of grain-surface formation and has sublimated into the gas phase during the outburst. DCO$^+$, DCN, and C$_2$D are products of gas-phase chemistry, their deuterium enhancement could still be ongoing in the cold layers of the envelope.

The study of outbursting objects is crucial to understand to which extent bursts sublimate and reset icy grain mantles and influence the ice and gas-phase chemical inventory of future planet-forming material by sublimating species that would otherwise remain on the icy grains. These kind of bursts may completely alter the balance between inheritance and reconstitution of the volatile reservoirs during the formation of protoplanetary systems. Investigating the chemical composition of VeLLOs allows the study of objects at the low luminosity and low mass end of star formation, which has been understudied so far. The APEX data have revealed that VeLLOs, at least the one in DC3272+18, is rich in molecules. To fully understand their chemical composition it is necessary to obtain observations with a higher spatial resolution with facilities such as ALMA. This will allow the emission of molecules to be spatially resolved, and also for the existence of a hot corino to be probed, where COMs are expected to be in the gas phase, if the chemical composition in VeLLOs is in line with what is found around low-mass protostars, just at closer distances to the central star due to its lower luminosity. Complementary observations with the *James Webb* Space Telescope would offer the opportunity to study the level of reprocessing of the ices induced by the past outburst.

References

Ahrens, V., Lewen, F., Takano, S., et al. 2002, Z. Naturforsch. Teil A, 57, 669
Amano, T., Hirao, T., & Takano, J. 2005, J. Mol. Spectrosc., 234, 170

Ambrose, H. E., Shirley, Y. L., & Scibelli, S. 2021, MNRAS, 501, 347
André, P., Motte, F., & Bacmann, A. 1999, ApJ, 513, L57
Andrews, S. M., Huang, J., Pérez, L. M., et al. 2018, ApJ, 869, L41
Asvany, O., Schlemmer, S., & Gerlich, D. 2004, ApJ, 617, 685
Bacmann, A., Taquet, V., Faure, A., Kahane, C., & Ceccarelli, C. 2012, A&A, 541, L12
Baulch, D. L., Bowman, C. T., Cobos, C. J., et al. 2005, J. Phys. Chem. Ref. Data, 34, 757
Belloche, A., Parise, B., van der Tak, F. F. S., et al. 2006, A&A, 454, L51
Belloche, A., Maury, A. J., Maret, S., et al. 2020, A&A, 635, A198
Betts, J., & Back, R. A. 1965, Can. J. Chem., 43, 2678
Bianchi, E., Codella, C., Ceccarelli, C., et al. 2017, MNRAS, 467, 3011
Bizzocchi, L., Caselli, P., Spezzano, S., & Leonardo, E. 2014, A&A, 569, A27
Blackman, G. L., Brown, R. D., Godfrey, P. D., & Gunn, H. I. 1976, Nature, 261, 395
Blake, G. A., Sutton, E. C., Masson, C. R., & Phillips, T. G. 1987, ApJ, 315, 621
Bocquet, R., Demaison, J., Cosléou, J., et al. 1999, J. Mol. Spectrosc., 195, 345
Bogey, M., Demuynck, C., & Destombes, J. L. 1986, Chem. Phys. Lett., 125, 383
Bogey, M., Demuynck, C., Destombes, J. L., & Dubus, H. 1987, J. Mol. Spectrosc., 122, 313
Bogey, M., Civiš, S., Delcroix, B., et al. 1997, J. Mol. Spectrosc., 182, 85
Boogert, A. C. A., Gerakines, P. A., & Whittet, D. C. B. 2015, ARA&A, 53, 541
Botschwina, P., Horn, M., Flügge, J., & Seeger, S. 1993, J. Chem. Soc. Faraday Trans., 89, 2219
Bourke, T .L., Myers, P. C., Evans, N. J.I, et al. 2006, ApJ, 649, L37
Brünken, S., Fuchs, U., Lewen, F., et al. 2004, J. Mol. Spectrosc., 225, 152
Brunken, N. G. C., Booth, A. S., Leemker, M., et al. 2022, A&A, 659, A29
Cabezas, C., Agúndez, M., Marcelino, N., et al. 2021, A&A, 654, A45
Caselli, P., & Ceccarelli, C. 2012, A&ARv, 20, 56
Caselli, P., & Dore, L. 2005, A&A, 433, 1145
Cazzoli, G., Puzzarini, C., & Lapinov, A. V. 2004, ApJ, 611, 615
Ceccarelli, C., Caselli, P., Herbst, E., Tielens, A. G. G. M., et al. 2007, Protostars and Planets (University of Arizona Press), 47
Chacón-Tanarro, A., Caselli, P., Bizzocchi, L., et al. 2019, A&A, 622, A141
Codella, C., Viti, S., Lefloch, B., et al. 2018, MNRAS, 474, 5694
Collings, M. P., Anderson, M. A., Chen, R., et al. 2004, MNRAS, 354, 1133
Congiu, E., Chaabouni, H., Laffon, C., et al. 2012, J. Chem. Phys., 137, 054713
DeLeon, R. L., & Muenter, J. S. 1984, J. Chem. Phys., 80, 3992
di Francesco, J., Evans, N. J., I., Caselli, P., , et al. 2007, Protostars and Planets V (University of Arizona Press), 17
Dore, L., Caselli, P., Beninati, S., et al. 2004, A&A, 413, 1177
Drozdovskaya, M. N., Coudert, L. H., Margulès, L., et al. 2022, A&A, 659, A69
Dumke, M., & Mac-Auliffe, F. 2010, Proc. SPIE, 7737, 77371J
Dunham, M. M., Evans, N. I, Bourke, T. L., et al. 2006, ApJ, 651, 945
Dunham, M. M., Crapsi, A., & Evans, N. I 2008, ApJS, 179, 249
Dunham, M. M., Evans, N. J., Bourke, T. L., et al. 2010a, ApJ, 721, 995
Dunham, M. M., Evans, N., Terebey, S. I, Dullemond, C. P., et al. 2010b, ApJ, 710, 470
Ebenstein, W. L., & Muenter, J. S. 1984, J. Chem. Phys., 80, 3989
Endres, C. P., Schlemmer, S., Schilke, P., Stutzki, J., & Müller, H. S. P. 2016, J. Mol. Spectrosc., 327, 95
Enoch, M. L., Evans, I., N., Sargent, A. I., & Glenn, J. 2009, ApJ, 692, 973
Evans, N.I, Allen, L. E., & Blake, G. A. 2003, PASP, 115, 965
Fabricant, B., Krieger, D., & Muenter, J. S. 1977, J. Chem. Phys., 67, 1576
Favre, C., Bergin, E. A., Cleeves, L. I., et al. 2015, ApJ, 802, L23
Favre, C., Vastel, C., Jimenez-Serra, I., et al. 2020, A&A, 635, A189
Fedoseev, G., Ioppolo, S., Lamberts, T., et al. 2012, J. Chem. Phys., 137, 054714
Fedoseev, G., Chuang, K. J., van Dishoeck, E. F., Ioppolo, S., & Linnartz, H. 2016, MNRAS, 460, 4297
Foreman-Mackey, D., Hogg, D. W., Lang, D., & Goodman, J. 2013, PASP, 125, 306
Frimann, S., Jørgensen, J. K., Dunham, M. M., et al. 2017, A&A, 602, A120
Garrod, R. T., & Herbst, E. 2006, A&A, 457, 927
Garrod, R. T., Widicus Weaver, S. L., & Herbst, E. 2008, ApJ, 682, 283
Gericke, K. H., Lock, M., Schmidt, F., & Comes, F. J. 1994, J. Chem. Phys., 101, 1988
Gerin, M., Viala, Y., & Casoli, F. 1993, A&A, 268, 212
Goldsmith, P. F., & Langer, W. D. 1999, ApJ, 517, 209
Goorvitch, D. 1994, ApJS, 95, 535
Hacar, A., Bosman, A. D., & van Dishoeck, E. F. 2020, A&A, 635, A4
Halfen, D. T., Apponi, A. J., & Ziurys, L. M. 2001, ApJ, 561, 244
Heays, A. N., Bosman, A. D., & van Dishoeck, E. F. 2017, A&A, 602, A105
Herbst, E., & van Dishoeck, E. F. 2009, ARA&A, 47, 427
Herbst, E., Adams, N. G., Smith, D., & Defrees, D. J. 1987, ApJ, 312, 351
Hidaka, H., Watanabe, M., Kouchi, A., & Watanabe, N. 2009, ApJ, 702, 291
Hsieh, T.-H., Lai, S.-P., Belloche, A., Wyrowski, F., & Hung, C.-L. 2015, ApJ, 802, 126

Hsieh, T.-H., Murillo, N. M., Belloche, A., et al. 2018, ApJ, 854, 15
Hsieh, T.-H., Murillo, N. M., Belloche, A., et al. 2019, ApJ, 884, 149
Jiménez-Serra, I., Vasyunin, A. I., Caselli, P., et al. 2016, ApJ, 830, L6
Jiménez-Serra, I., Vasyunin, A. I., Spezzano, S., et al. 2021, ApJ, 917, 44
Jørgensen, J. K., Schöier, F. L., & van Dishoeck, E. F. 2005, A&A, 435, 177
Jørgensen, J. K., van der Wiel, M. H. D., Coutens, A., et al. 2016, A&A, 595, A117
Jørgensen, J. K., Müller, H. S. P., Calcutt, H., et al. 2018, A&A, 620, A170
Kauffmann, J., Bertoldi, F., Bourke, T. L., et al. 2011, MNRAS, 416, 2341
Kenyon, S. J., & Hartmann, L. 1995, ApJS, 101, 117
Kim, G., Lee, C. W., Maheswar, G., et al. 2019, ApJS, 240, 18
Kim, M.-R., Lee, C. W., Maheswar, G., Myers, P. C., & Kim, G. 2021, ApJ, 910, 112
Klapper, G., Lewen, F., Gendriesch, R., Belov, S. P., & Winnewisser, G. 2000, J. Mol. Spectrosc., 201, 124
Klapper, G., Lewen, F., Gendriesch, R., Belov, S. P., & Winnewisser, G. 2001, Z. Naturforschung Teil A, 56, 329
Klapper, G., Surin, L., Lewen, F., et al. 2003, ApJ, 582, 262
Lattanzi, V., Walters, A., Drouin, B. J., & Pearson, J. C. 2007, ApJ, 662, 771
Lattanzi, V., Bizzocchi, L., Vasyunin, A. I., et al. 2020, A&A, 633, A118
Lee, C. W., Bourke, T. L., Myers, P. C., et al. 2009, ApJ, 693, 1290
Lee, C. W., Kim, M.-R., Kim, G., et al. 2013, ApJ, 777, 50
Leemker, M., Booth, A. S., van Dishoeck, E. F., et al. 2023, A&A, 673, A7
Ligterink, N. F. W., Calcutt, H., Coutens, A., et al. 2018, A&A, 619, A28
Ligterink, N. F. W., & Minissale, M. 2023, A&A, 676, A80
Lin, Y., Spezzano, S., & Caselli, P. 2023, A&A, 669, L6
Linsky, J. L., Draine, B. T., Moos, H. W., et al. 2006, ApJ, 647, 1106
Liszt, H. S., & Turner, B. E. 1978, ApJ, 224, L73
Lovas, F. J., Suenram, R. D., Ogata, T., & Yamamoto, S. 1992, ApJ, 399, 325
Maureira, M. J., Pineda, J. E., Liu, H. B., et al. 2024, A&A, 689, L5
McGonagle, D., Ziurys, L. M., Irvine, W. M., & Minh, Y. C. 1990, ApJ, 359, 121
Megías, A., Jiménez-Serra, I., Martín-Pintado, J., et al. 2023, MNRAS, 519, 1601
Millar, T. J., Bennett, A., & Herbst, E. 1989, ApJ, 340, 906
Millar, T. J., Bennett, A., Rawlings, J. M. C., Brown, P. D., & Charnley, S. B. 1991, A&AS, 87, 585
Minissale, M., Aikawa, Y., Bergin, E., et al. 2022, ACS Earth Space Chem., 6, 597
Möllmann, E., Maki, A. G., Winnewisser, M., Winnewisser, B. P., & Quapp, W. 2002, J. Mol. Spectrosc., 212, 22
Müller, H. S. P., & Brünken, S. 2005, J. Mol. Spectrosc., 232, 213
Müller, H. S. P., & Lewen, F. 2017, J. Mol. Spectrosc., 331, 28
Müller, H. S. P., Gendriesch, R., Margulès, L., et al. 2000, Phys. Chem. Chem. Phys., 2, 3401
Müller, H. S. P., Schlöder, F., Stutzki, J., & Winnewisser, G. 2005, J. Mol. Struct., 742, 215
Müller, H. S. P., Spezzano, S., Bizzocchi, L., et al. 2013, J. Phys. Chem. A, 117, 13843
Müller, H. S. P., Kobayashi, K., Takahashi, K., Tomaru, K., & Matsushima, F. 2015, J. Mol. Spectrosc., 310, 92
Murillo, N. M., Bruderer, S., van Dishoeck, E. F., et al. 2015, A&A, 579, A114
Murillo, N. M., van Dishoeck, E. F., Tobin, J. J., Mottram, J. C., & Karska, A. 2018, A&A, 620, A30
Nagaoka, A., Watanabe, N., & Kouchi, A. 2007, J. Phys. Chem. A, 111, 3016
Pagani, L., Daniel, F., & Dubernet, M. L. 2009, A&A, 494, 719
Palau, A., Zapata, L. A., Rodríguez, L. F., et al. 2014, MNRAS, 444, 833
Pantaleone, S., Enrique-Romero, J., Ceccarelli, C., et al. 2020, ApJ, 897, 56

Patel, D., Margolese, D., & Dyke, T. R. 1979, J. Chem. Phys., 70, 2740
Pearson, J. C., Yu, S., & Drouin, B. J. 2012, J. Mol. Spectrosc., 280, 119
Pickett, H. M., Poynter, R. L., Cohen, E. A., et al. 1998, J. Quant. Spectr. Rad. Transf., 60, 883
Prodanović, T., Steigman, G., & Fields, B. D. 2010, MNRAS, 406, 1108
Raymonda, J. W., Muenter, J. S., & Klemperer, W. A. 1970, J. Chem. Phys., 52, 3458
Roueff, E., & Lique, F. 2013, Chem. Rev., 113, 8906
Sakai, N., & Yamamoto, S. 2013, Chem. Rev., 113, 8981
Saykally, R. J., Szanto, P. G., Anderson, T. G., & Woods, R. C. 1976, ApJ, 204, L143
Scholz, A., Froebrich, D., & Wood, K. 2013, MNRAS, 430, 2910
Scibelli, S., & Shirley, Y. 2020, ApJ, 891, 73
Segura-Cox, D. M., Schmiedeke, A., Pineda, J. E., et al. 2020, Nature, 586, 228
Shu, F. H., Adams, F. C., & Lizano, S. 1987, ARA&A, 25, 23
Sipilä, O., Silsbee, K., & Caselli, P. 2021, ApJ, 922, 126
Spezzano, S., Tamassia, F., Thorwirth, S., et al. 2012, ApJS, 200, 1
Tabone, B., Cabrit, S., Bianchi, E., et al. 2017, A&A, 607, L6
Tabone, B., Godard, B., Pineau des Forêts, G., Cabrit, S., et al. 2020, A&A, 636, A60
Takahashi, S., Ohashi, N., & Bourke, T. L. 2013, ApJ, 774, 20
Thorwirth, S., Müller, H. S. P., Lewen, F., et al. 2003, ApJ, 585, L163
Tinti, F., Bizzocchi, L., Degli Esposti, C., & Dore, L. 2007, ApJ, 669, L113
Tobin, J.J., van 't Hoff, M.L.R., & Leemker, M. 2023, Nature, 615, 227
Tychoniec, Ł., Manara, C. F., Rosotti, G. P., et al. 2020, A&A, 640, A19
Tychoniec, Ł., van Dishoeck, E. F., van 't Hoff, M. L. R., et al. 2021, A&A, 655, A65
Väisälä, M. S., Harju, J., Mantere, M. J., et al. 2014, A&A, 564, A99
van der Marel, N., Dong, R., di Francesco, J., Williams, J. P., & Tobin, J. 2019, ApJ, 872, 112
van der Tak, F. F. S., Müller, H. S. P., Harding, M. E., & Gauss, J. 2009, A&A, 507, 347
van Dishoeck, E. F., Jonkheid, B., & van Hemert, M. C. 2006, Faraday Discussions, 133, 231
Vastel, C., Bottinelli, S., Caux, E., Glorian, J.M., Boiziot, M., et al. 2015, Proc. Annual Meeting of the French Society of Astronomy and Astrophysics, 313
Vasyunin, A. I., Caselli, P., Dulieu, F., & Jiménez-Serra, I. 2017, ApJ, 842, 33
Virtanen, P., Gommers, R., Oliphant, T. E., et al. 2020, Nat. Methods, 17, 261
Visser, R., Bergin, E. A., & Jørgensen, J. K. 2015, A&A, 577, A102
Vrtilek, J. M., Gottlieb, C. A., & Thaddeus, P. 1987, ApJ, 314, 716
Wakelam, V., Herbst, E., Loison, J. C., et al. 2012, ApJS, 199, 21
Wakelam, V., Loison, J. C., Mereau, R., & Ruaud, M. 2017, Mol. Astrophys., 6, 22
Watson, W. D. 1974, ApJ, 188, 35
Willacy, K. 2007, ApJ, 660, 441
Winnewisser, M., Winnewisser, B. P., & Winnewisser, G. 1985, NATO Advanced Study Institute (ASI). Series C, 157, 375
Winnewisser, G., Belov, S. P., Klaus, T., & Schieder, R. 1997, J. Mol. Spectrosc., 184, 468
Xu, L.-H., Fisher, J., Lees, R. M., et al. 2008, J. Mol. Spectrosc., 251, 305
Yang, Y.-L., Sakai, N., Zhang, Y., et al. 2021, ApJ, 910, 20
Yıldız, U. A., Acharyya, K., Goldsmith, P. F., et al. 2013, A&A, 558, A58
Yoshida, K., Sakai, N., Nishimura, Y., et al. 2019, PASJ, 71, S18
Young, C. H., Jørgensen, J. K., Shirley, Y. L., et al. 2004, ApJS, 154, 396
Zink, L. R., De Natale, P., Pavone, F. S., et al. 1990, J. Mol. Spectrosc., 143, 304
Ziurys, L. M., Apponi, A. J., Hollis, J. M., & Snyder, L. E. 1994, ApJ, 436, L181
Zwicky, L., Molyarova, T., Akimkin, V., et al. 2024, MNRAS, 527, 7652

Appendix A: Spectra and parameters of the detected lines

The spectra of all securely and tentatively detected lines (Table A.1) are shown in Figs. A.1 and A.2 and are overlaid with Gaussian fits in red. All fits were obtained in CLASS and with the CURVE_FIT module in SCIPY (Virtanen et al. 2020), the rms displayed in the plots are taken from Table A.1. In Fig. A.1, velocity binning over two channels was applied to the D_2CO line, and the SO_2 line at 235.151 GHz, and for the NO transition at 250.475 GHz and the SO_2 transition at 236.217 GHz in Fig. A.2.

Appendix B: Spectra of notable non-detections

Fig. B.1 shows the spectral window with the non-detections of the SiO line at 217.105 GHz, the $^{13}C^{17}O$ line at 214.574 GHz, the $H_2^{13}CO$ line at 219.909 GHz, and two CH_2DOH transitions at 214.702 and 253.629 GHz that were searched for in the data based on their similar upper state energies, and line strengths compared to detected species. Velocity-binning over two channels was applied to both CH_2DOH transitions and the $H_2^{13}CO$ line.

Appendix C: Spectroscopic parameters

Table C.2 lists whether the spectroscopic data was taken from JPL or CDMS, and lists the papers that the catalog entries are based on.

Table A.1. Observed molecular transitions in this work.

Molecule	Transition	Frequency (GHz)	E_{up} (K)	A_{ij} (s^{-1})	$T_{mb,peak}$ [b] (K)	Δv [b] (km s^{-1})	v_{LSR} [b] (km s^{-1})	T_{rms} (mK)
CO	2-1	230.53800	16.60	6.91×10^{-7}	4.656	2.14 ± 0.03	-0.30 ± 0.01	65.9
^{13}CO[a]	2-1	220.39863	15.87	6.08×10^{-7}	4.089	0.75 ± 0.01	-0.16 ± 0.01	8.3
					1.529	0.53 ± 0.02	0.38 ± 0.01	
C^{18}O	2-1	219.56035	15.81	6.01×10^{-7}	2.227	0.54 ± 0.00	-0.01 ± 0.00	3.6
N$_2$D$^+$ [c]	3-2	231.32186	22.20	7.14×10^{-4}	0.142	0.42 ± 0.02	-0.24 ± 0.01	4.6
	3-2	231.31996	22.20	6.65×10^{-5}	0.016	0.31 ± 0.06	2.29 ± 0.03 [d]	4.6
	3-2	231.32145	22.20	6.00×10^{-4}	0.034	0.49 ± 0.08	0.28 ± 0.03 [d]	4.6
	3-2	231.32444	22.20	9.87×10^{-5}	0.009	0.28 ± 0.11	-3.48 ± 0.05 [d]	4.6
HCO$^+$	3-2	267.55753	25.68	1.45×10^{-3}	1.480	0.65 ± 0.00	-0.32 ± 0.00	6.2
DCO$^+$	3-2	216.11258	20.74	7.66×10^{-4}	0.559	0.43 ± 0.00	0.0 ± 0.0	2.7
HCN[c]	3-2	265.88618	25.52	8.36×10^{-4}	0.259	0.67 ± 0.02	-0.50 ± 0.01	5.4
	3-2	265.88852	25.52	3.10×10^{-5}	0.040	0.41 ± 0.08	-2.83 ± 0.03	5.4
	3-2	265.88489	25.52	3.09×10^{-5}	0.138	0.41 ± 0.02	1.29 ± 0.01	7.6
DCN[b]	3-2	217.23863	20.85	4.58×10^{-4}	0.033	0.40 ± 0.06	0.08 ± 0.04	3.2
	3-2	217.23823	20.85	9.15×10^{-5}	0.010	0.49 ± 0.28	0.53 ± 0.16	3.2
HNC	3-2	271.98114	26.61	9.34×10^{-4}	0.970	0.57 ± 0.01	-0.13 ± 0.00	5.9
H$_2$CO	$3_{0,3} - 2_{0,2}$	218.22219	20.96	2.82×10^{-4}	0.373	0.46 ± 0.00	0.03 ± 0.00	3.2
*CH$_3$OH	$4_{2,3} - 3_{1,2}$	218.44006	45.46	4.69×10^{-5}	0.013	0.26 ± 0.06	0.1 ± 0.03	3.8
CH$_3$OH	$2_{0,2} - 1_{1,1}$	254.01538	20.09	1.90×10^{-5}	0.081	0.38 ± 0.02	0.01 ± 0.01	6.5
NO	5/2-3/2	250.43685	19.23	1.84×10^{-6}	0.089	0.38 ± 0.02	-0.00 ± 0.01	5.3
NO	5/2-3/2	250.44066	19.23	1.55×10^{-6}	0.055	0.41 ± 0.08	-0.02 ± 0.02	5.1
NO	5/2-3/2	250.44853	19.23	1.38×10^{-6}	0.034	0.38 ± 0.06	-0.01 ± 0.03	5.1
*NO	5/2-3/2	250.47541	19.23	4.42×10^{-7}	0.016	0.37 ± 0.09	-0.01 ± 0.04	5.0
NO	5/2-3/2	250.79644	19.28	1.85×10^{-6}	0.094	0.41 ± 0.01	-0.06 ± 0.01	5.3
NO	5/2-3/2	250.81559	19.28	1.55×10^{-6}	0.055	0.42 ± 0.03	-0.49 ± 0.01	5.1
NO	5/2-3/2	250.81695	19.27	1.39×10^{-6}	0.032	0.45 ± 0.06	0.03 ± 0.00	5.1
c-C$_3$H$_2$	$3_{3,0} - 2_{2,1}$	216.27876	19.47	2.56×10^{-4}	0.111	0.45 ± 0.01	0.00 ± 0.01	3.4
c-C$_3$H$_2$	$6_{0,6} - 5_{1,5}$	217.82215	38.61	5.40×10^{-4}	0.034	0.53 ± 0.04	0.00 ± 0.02	4.2
c-C$_3$H$_2$	$5_{1,4} - 4_{2,3}$	217.94005	35.41	4.03×10^{-4}	0.017	0.51 ± 0.07	0.10 ± 0.03	3.6
*c-C$_3$H$_2$	$5_{2,3} - 4_{3,2}$	249.05437	41.02	4.16×10^{-4}	0.012	0.45 ± 0.16	-0.02 ± 0.05	5.2
c-C$_3$H$_2$	$6_{2,5} - 5_{1,4}$	251.52731	47.49	6.75×10^{-4}	0.015	0.37 ± 0.08	0.07 ± 0.05	4.5
c-C$_3$H$_2$	$4_{4,1} - 3_{3,0}$	265.75948	32.22	7.27×10^{-4}	0.022	0.45 ± 0.06	-0.10 ± 0.03	4.8
C$_2$D	$3_{4,5} - 2_{3,4}$	216.37284	20.77	2.99×10^{-5}	0.014	0.27 ± 0.06	0.07 ± 0.04	2.8
C$_2$D	$3_{4,3} - 2_{3,2}$	216.37331	20.77	2.67×10^{-5}	0.013	0.27 ± 0.07	0.04 ± 0.03	2.8
C$_2$D	$3_{4,4} - 2_{3,3}$	216.37332	20.77	2.76×10^{-5}	0.009	0.28 ± 0.06	-0.04 ± 0.02	2.8
C$_2$D	$3_{3,4} - 2_{2,3}$	216.42825	20.77	2.77×10^{-5}	0.010	0.38 ± 0.08	-0.02 ± 0.04	2.8
C$_2$D	$3_{3,3} - 2_{2,2}$	216.42843	20.77	2.33×10^{-5}	0.010	0.38 ± 0.08	0.22 ± 0.03	2.8
C$_2$D	$3_{3,2} - 2_{2,1}$	216.42888	20.77	2.09×10^{-5}	0.010	0.38 ± 0.09	0.75 ± 0.04	2.8
D$_2$CO	$4_{0,4} - 3_{0,3}$	231.41023	27.88	3.47×10^{-4}	0.012	0.36 ± 0.10	-0.24 ± 0.04	3.4
SO$_2$	$4_{2,2} - 3_{1,3}$	235.15172	19.03	7.69×10^{-5}	0.012	0.64 ± 0.13	-0.26 ± 0.05	3.5
*SO$_2$	$16_{1,15} - 15_{2,14}$	236.21669	130.67	7.50×10^{-5}	0.011	0.27 ± 0.13	0.04 ± 0.04	3.0
SO	5,5 - 4,4	215.22065	44.10	1.19×10^{-4}	0.018	0.58 ± 0.05	0.06 ± 0.02	2.6
SO	5,6 - 4,5	219.94944	34.98	1.34×10^{-4}	0.119	0.46 ± 0.01	0.01 ± 0.00	3.2
*SO	6,5 - 5,4	251.82577	50.66	1.92×10^{-4}	0.017	0.31 ± 0.11	-0.07 ± 0.04	5.6

Notes. Tentative detections are marked with an asterisk in front of the molecule name. The spectra and their fits are plotted in Figs. A.1 and A.2.
[a] ^{13}CO was fit with two Gaussians [b] The peak temperature, $T_{mb,peak}$, the line width of the spectral lines, Δv, and the v_{LSR}, and the T_{rms} of the data of the spectral lines were determined with a Gaussian fit with the CLASS package of the GILDAS software and the CURVE_FIT module of SCIPY (Virtanen et al. 2020); [c] hyperfine components were detected; [d] the position of the hyperfine transitions is given relative to the strongest transition (Fig. A.1).
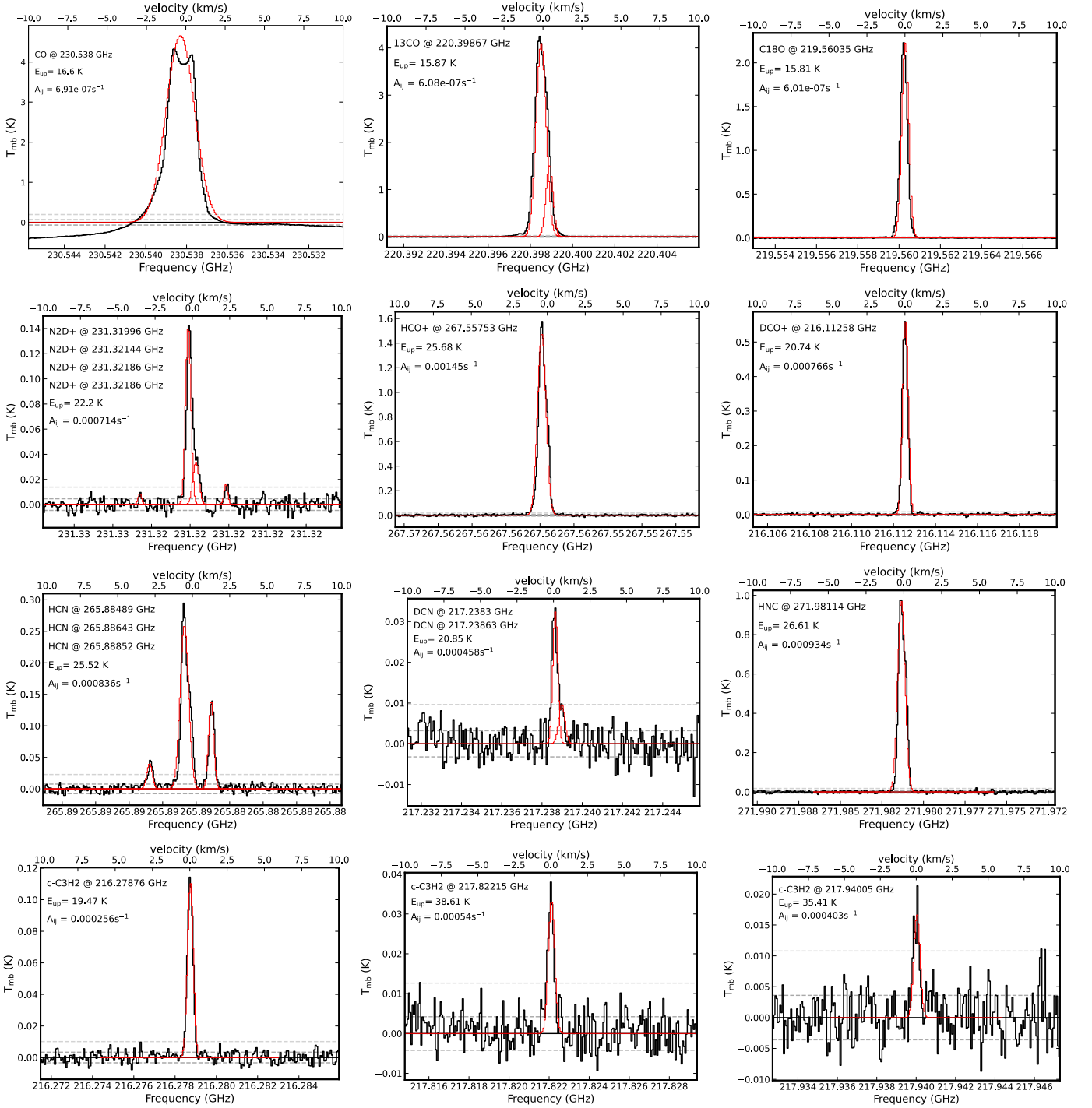
Fig. A.1. Spectra of the securely detected transitions (Table A.1) overlaid with the Gaussian best-fit model in red (Table A.1). Not all lines are perfectly fit by a Gaussian, kinematics or line broadening are factors that can influence the line shape, in the case of CO and ^{13}CO two components are used to fit the line. It is also to note that due to the large beam size of 26.2″ different physical components are not resolved, and emission is picked up from multiple components. The dashed, dark gray line indicates the 3×rms value, the dashed, light gray line indicates the rms value.
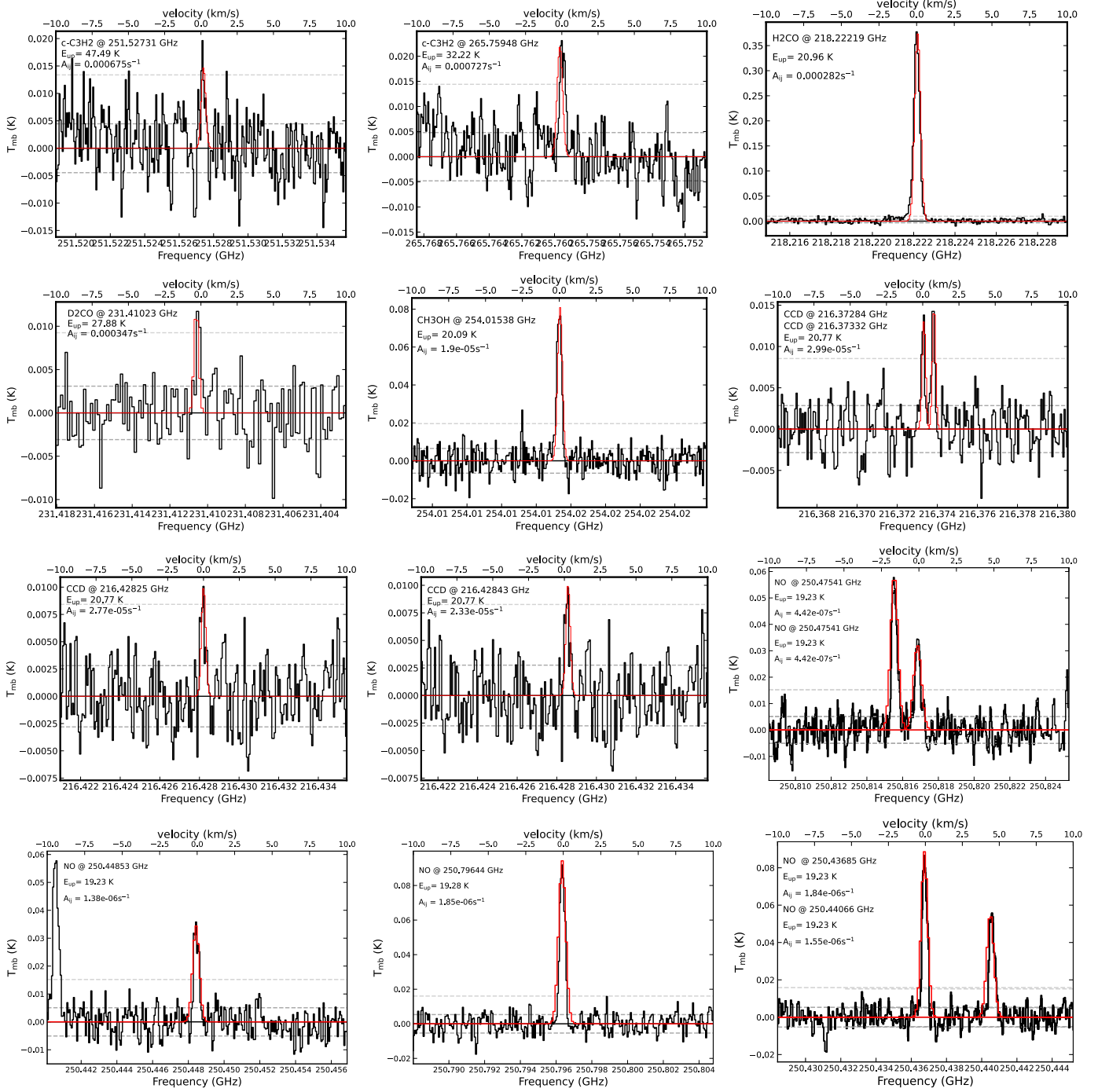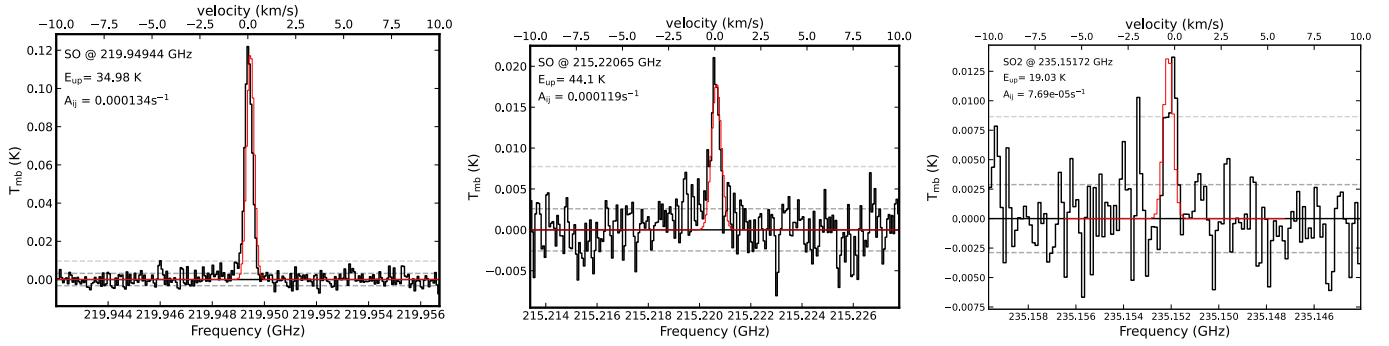
Fig. A.1. Continued.
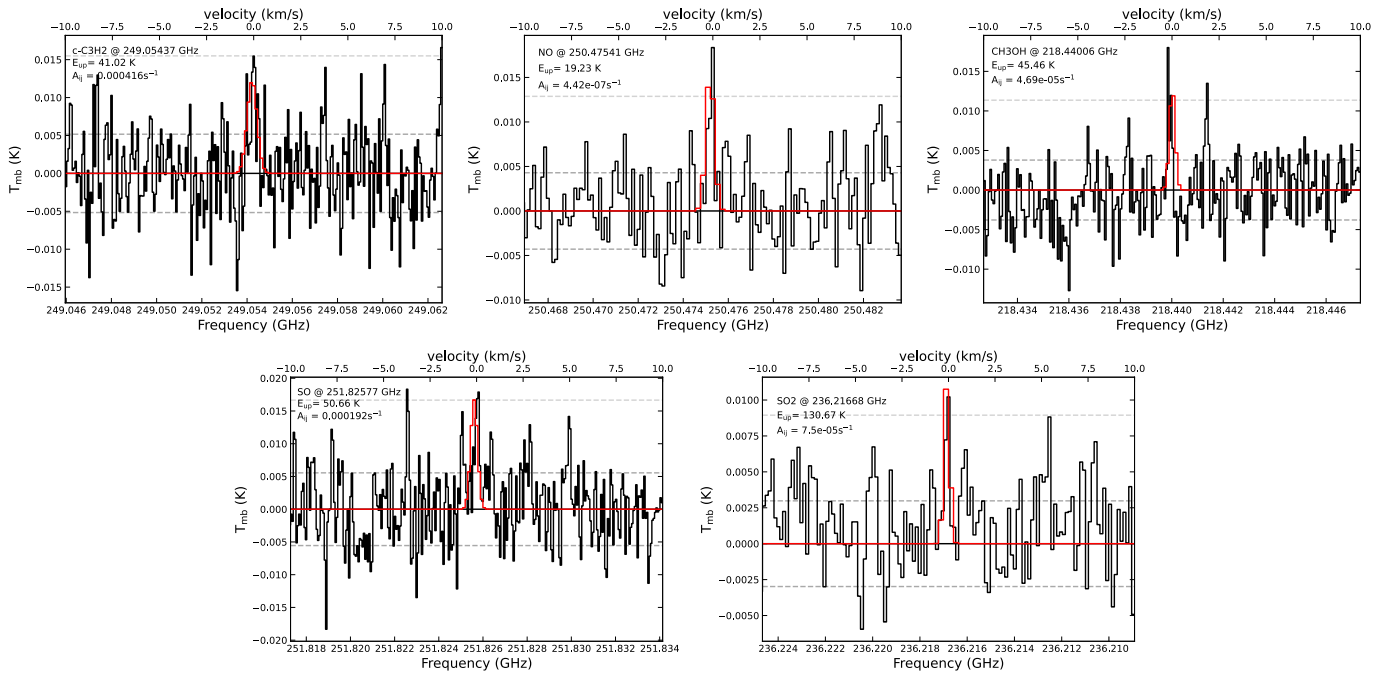
Fig. A.1. Continued.

Fig. A.2. Spectra of the tentatively detected transitions (Table A.1) overlaid with the Gaussian fit in red (Table A.1). The dashed, dark gray line indicates the 3×rms value, the dashed, light gray line indicates the rms value.
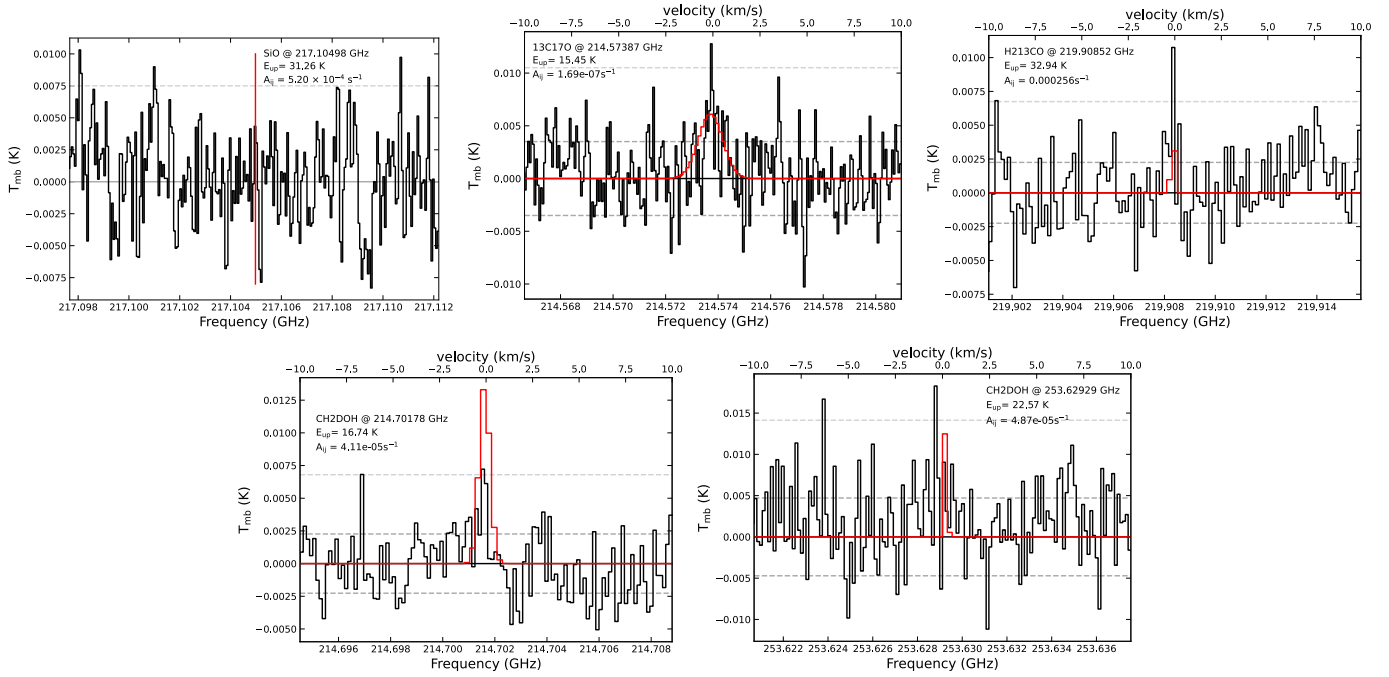
Fig. B.1. Notable non-detections in the data. The 3×rms value is indicated by the dashed, light gray line, the rms value is indicated by the dashed, dark gray line. The position of the targeted SiO transition is indicated by the red line, for the remaining lines the attempt to fit a Gaussian to the data is displayed in red.

Table C.1. Notable non-detections.

Molecule	Transition	Frequency (GHz)	E_{up} (K)	A_{ij} (s^{-1})
SiO	$5_0 - 4_0$	217.10492	31.26	5.20×10^{-4}
$^{13}C^{17}O$	2-1	214.57387	15.45	1.69×10^{-7}
$H_2^{13}CO$	$3_{1,2} - 2_{1,1}$	219.90853	32.98	2.56×10^{-4}
CH_2DOH	$3_{1,2} - 2_{1,1}$	214.70178	16.74	4.11×10^{-5}
CH_2DOH	$2_{2,1} - 2_{1,2}$	253.62929	22.57	4.87×10^{-5}

Table C.2. References to the spectroscopic data of all the molecules that were detected or searched for in the VeLLO in the DC3272+18 cloud and discussed in this work.

Molecule	Database	References
CO	CDMS	Goorvitch (1994), Winnewisser et al. (1997)
^{13}CO	CDMS	Zink et al. (1990), Goorvitch (1994), Klapper et al. (2000), Cazzoli et al. (2004)
$C^{18}O$	CDMS	Winnewisser et al. (1985), Goorvitch (1994), Klapper et al. (2001)
N_2D^+	CDMS	Dore et al. (2004), Amano et al. (2005), Pagani et al. (2009)
HCO^+	CDMS	Botschwina et al. (1993), Lattanzi et al. (2007), Tinti et al. (2007)
DCO^+	CDMS	Caselli & Dore (2005), Lattanzi et al. (2007), van der Tak et al. (2009)
HCN	CDMS	Ebenstein & Muenter (1984), Ahrens et al. (2002), Thorwirth et al. (2003)
DCN	CDMS	DeLeon & Muenter (1984), Möllmann et al. (2002), Brünken et al. (2004)
HNC	CDMS	Blackman et al. (1976), Saykally et al. (1976)
H_2CO	CDMS	Fabricant et al. (1977), Müller & Lewen (2017)
CH_3OH	CDMS	Xu et al. (2008)
NO	CDMS	Müller et al. (2015)
c-C_3H_2	CDMS	Bogey et al. (1986, 1987), Vrtilek et al. (1987), Lovas et al. (1992), Spezzano et al. (2012)
C_2D	CDMS	Yoshida et al. (2019), Cabezas et al. (2021)
D_2CO	CDMS	Fabricant et al. (1977), Bocquet et al. (1999)
SO_2	CDMS	Patel et al. (1979), Müller & Brünken (2005)
SO	CDMS	Lovas et al. (1992), Bogey et al. (1997)
SiO	CDMS	Raymonda et al. (1970), Müller et al. (2013)
$^{13}C^{17}O$	CDMS	Goorvitch (1994), Klapper et al. (2003)
$H_2^{13}CO$	CDMS	Fabricant et al. (1977), Müller et al. (2000)
CH_2DOH	JPL	Pearson et al. (2012)